JBC ARTICLE

Author's Choice

Negatively charged residues in the first extracellular loop of the L-type $Ca_V1.2$ channel anchor the interaction with the $Ca_V\alpha2\delta1$ auxiliary subunit

Received for publication, July 14, 2017, and in revised form, August 18, 2017 Published, Papers in Press, September 1, 2017, DOI 10.1074/jbc.M117.806893

Benoîte Bourdin[‡1], **Julie Briot**[‡§1], **Marie-Philippe Tétreault**[‡], **Rémy Sauvé**[§], **and Lucie Parent**[‡§2]

From the [§]*Département de Pharmacologie et Physiologie, Faculté de Médecine, and* [‡]*Centre de Recherche de l'Institut de Cardiologie de Montréal, Université de Montréal, Montréal, Québec H3C 3J7, Canada*

Edited by Roger J. Colbran

Voltage-gated L-type $Ca_V1.2$ channels in cardiomyocytes exist as heteromeric complexes. Co-expression of $Ca_V\alpha2\delta1$ with $Ca_V\beta$/$Ca_V\alpha1$ proteins reconstitutes the functional properties of native L-type currents, but the interacting domains at the $Ca_V1.2$/$Ca_V\alpha2\delta1$ interface are unknown. Here, a homology-based model of $Ca_V1.2$ identified protein interfaces between the extracellular domain of $Ca_V\alpha2\delta1$ and the extracellular loops of the $Ca_V\alpha1$ protein in repeats I (IS1S2 and IS5S6), II (IIS5S6), and III (IIIS5S6). Insertion of a 9-residue hemagglutinin epitope in IS1S2, but not in IS5S6 or in IIS5S6, prevented the co-immunoprecipitation of $Ca_V1.2$ with $Ca_V\alpha2\delta1$. IS1S2 contains a cluster of three conserved negatively charged residues Glu-179, Asp-180, and Asp-181 that could contribute to non-bonded interactions with $Ca_V\alpha2\delta1$. Substitutions of $Ca_V1.2$ Asp-181 impaired the co-immunoprecipitation of $Ca_V\beta$/$Ca_V1.2$ with $Ca_V\alpha2\delta1$ and the $Ca_V\alpha2\delta1$-dependent shift in voltage-dependent activation gating. In contrast, single substitutions in $Ca_V1.2$ in neighboring positions in the same loop (179, 180, and 182–184) did not significantly alter the functional up-regulation of $Ca_V1.2$ whole-cell currents. However, a negatively charged residue at position 180 was necessary to convey the $Ca_V\alpha2\delta1$-mediated shift in the activation gating. We also found a more modest contribution from the positively charged Arg-1119 in the extracellular pore region in repeat III of $Ca_V1.2$. We conclude that $Ca_V1.2$ Asp-181 anchors the physical interaction that facilitates the $Ca_V\alpha2\delta1$-mediated functional modulation of $Ca_V1.2$ currents. By stabilizing the first extracellular loop of $Ca_V1.2$, $Ca_V\alpha2\delta1$ may up-regulate currents by promoting conformations of the voltage sensor that are associated with the channel's open state.

In cardiac cells, Ca^{2+} signals control the force necessary for the myocardium to meet the physiological needs of the body (1). The primary pathway for Ca^{2+} influx in the adult heart is via the L-type Ca^{2+} channel. This Ca^{2+} influx pathway is essential for triggering sarcoplasmic reticulum Ca^{2+} release and is the major source of Ca^{2+} load in this organelle (2). Regulation of the L-type Ca^{2+} current has profound physiological significance. Alterations in density or the activation/inactivation gating of L-type $Ca_V1.2$ channels have been implicated in hypertrophic signaling (3) and in a variety of cardiovascular diseases such as hypertension (4), atrial fibrillation (5–8), heart failure (9, 10), and congenital arrhythmias (11–13).

Cardiac L-type $Ca_V1.2$ channels are heteromultimeric protein complexes formed by the pore-forming $Ca_V\alpha1$ subunit bound to the cytoplasmic $Ca_V\beta$ auxiliary subunit (14) with nanomolar affinity (15) and to the extracellular $Ca_V\alpha2\delta1$ subunit (16–20). The $Ca_V\alpha1$ subunit is formed by a single polypeptide chain of 24 transmembrane helices grouped into four structural homologous repeats (repeats I, II, II, and IV). $Ca_V\beta$ promotes the cell-surface trafficking of $Ca_V1.2$ channels through a single high-affinity binding site anchored on a tryptophan residue located in an intracellular helix linking repeats I and II of $Ca_V\alpha1$ (21).

Co-expression of $Ca_V\alpha2\delta1$ with $Ca_V\beta$-bound $Ca_V\alpha1$ increases by up to 10-fold the peak current density and promotes the activation of $Ca_V1.2$ at physiological voltages (22–27). The molecular determinants responsible for this modulation, and whether it involves a direct or an allosteric interaction, have yet to be identified. The three-dimensional (3D) structure of the homologous skeletal muscle $Ca_V1.1$ channel from rabbit, solved by single particle cryo-electron microscopy (cryo-EM) (20, 28), proposes multiple protein interfaces between the two proteins (Fig. 1). Many clusters of residues within the extracellular von Willebrand factor A (VWA)[3] and the cache1 domains of $Ca_V\alpha2\delta1$ could form interactions with extracellular loops from repeats I–III of the $Ca_V\alpha1$ subunit of $Ca_V1.2$. In particular, the polar residues Asp-261, Ser-263, Ser-265, Thr-333, and Asp-365 in the rabbit $Ca_V\alpha2\delta1$ are forming the metal-ion-dependent adhesion site (MIDAS), which are purported to play important roles at the protein interface. These $Ca_V\alpha2\delta1$ resi-

This work was supported by Operating Grant 130256 from the Canadian Institutes of Health Research and Grant-in-aid G-15-0009329 from the Canadian Heart and Stroke Foundation (to L. P.). The authors declare that they have no conflicts of interest with the contents of this article.

[1] Both authors contributed equally to this work.

[2] To whom correspondence should be addressed: Dépt. de Pharmacologie et Physiologie, Université de Montréal, P. O. Box 6128, Downtown Station, Montréal, Quebec H3C 3J7, Canada. Tel.: 514-343-6673; E-mail: lucie.parent@umontreal.ca.

[3] The abbreviations used are: VWA, von Willebrand factor A; AID, α-interacting domain; BTX, bungarotoxin; ΔG_{act}, free energy of activation; HEKT, human embryonic kidney 293 cells stably expressing an SV40 temperature-sensitive T antigen; MIDAS, metal-ion-dependent adhesion site; ΔMedFI, relative median fluorescent intensity; ANOVA, analysis of variance; pF, picofarad; DOPE, discrete optimized protein energy; PDB, Protein Data Bank.

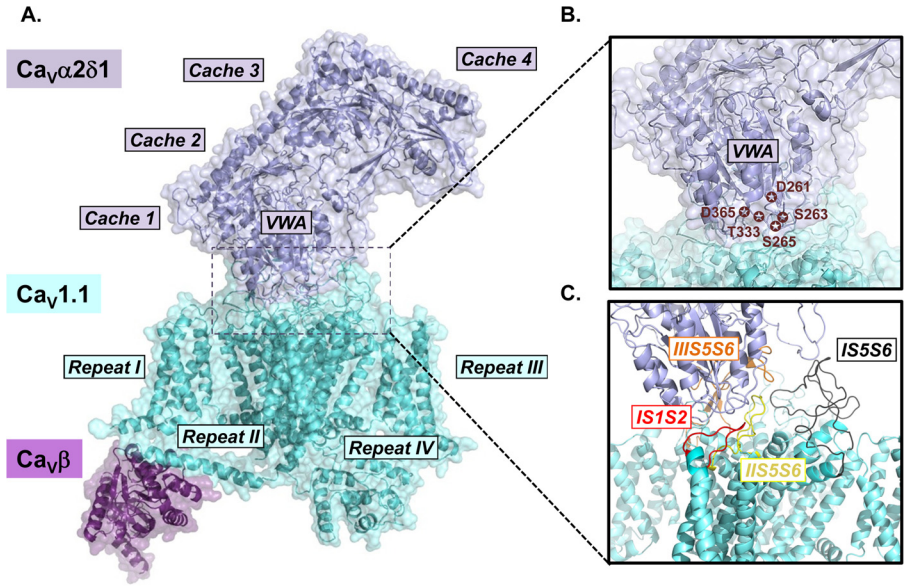

Figure 1. Three-dimensional cryo-electron microscopy structure of the $Ca_V1.1$ channel. *A*, surface representation of the rabbit $Ca_V1.1$ channel (*cyan*) in complex with $Ca_V\alpha2\delta1$ (*deep blue*) and $Ca_V\beta2$ (*violet*) (PDB: 5GJV). The structural domains of $Ca_V\alpha2\delta1$ and the relative orientation of repeats I–IV in the pore-forming $Ca_V\alpha1$ subunit of $Ca_V1.1$ are identified. For the correlation between the primary sequence and the structural domains of $Ca_V\alpha2\delta1$, see Fig. 2 in Ref. 56. The extensive interface between the two proteins is surrounded by a *dashed black square*, and this region is shown enlarged in *B* and *C*. *B*, structural details of the VWA domain of $Ca_V\alpha2\delta1$ are emphasized, and the residues forming the MIDAS are identified by *stars*. *C*, extracellular loops of $Ca_V1.1$ forming the interface with $Ca_V\alpha2\delta1$ are shown. Only the main chains are shown. The S1S2 loop in repeat I (IS1S2, residues 71–82) is in *red*; the turret and external pore region S5S6 in repeat I (IS5S6, residues 219–278) is in *black*; the turret and external pore region S5S6 in repeat II (IIS5S6, residues 581–600) is in *yellow*, and the turret and external pore region S5S6 in repeat III (IIIS5S6, residues 950–998) is in *orange*. Images were produced with PyMOL (Molecular Graphics System, Version 1.8 Schrödinger, LLC).

dues are facing residues in the extracellular loop linking the transmembrane helices S1 and S2 in the voltage sensor domain of repeat I (IS1S2) and the extracellular regions in the pore domains of repeats II and III (IIS5S6 and IIIS5S6, respectively), suggesting a broader interface than the highly localized α-interacting domain (AID) identified between $Ca_V1.2$ and $Ca_V\beta$ (15, 21, 29).

In this work, we sought to identify the "hot spot AID" at the $Ca_V1.2$/$Ca_V\alpha2\delta1$ interface using a combination of protein chemistry, molecular modeling, and functional characterization of channel mutants. Structural alterations in the first extracellular loop in repeat I of $Ca_V1.2$, by the insertion of the 9-residue human influenza hemagglutinin (HA = YPYDVPDYA) epitope, impaired the up-regulation of $Ca_V1.2$ currents by $Ca_V\alpha2\delta1$ and significantly decreased the co-immunoprecipitation of the two proteins. Single-point mutations of Asp-181 located within a conserved cluster of negatively charged residues (Glu-Asp-Asp or EDD) in the first extracellular loop of $Ca_V1.2$ prevented the modulation of whole-cell currents and the co-immunoprecipitation of the two proteins. These data contrast with the modest impact of point mutations in the extracellular loop between the 5th and the 6th transmembrane helices in repeat III of $Ca_V1.2$. Altogether, our data are compatible with a model where negatively charged aspartate residues in IS1S2 of $Ca_V1.2$ anchor the interaction with $Ca_V\alpha2\delta1$.

Results

Mapping the functional interface between $Ca_V1.2$ and $Ca_V\alpha2\delta1$

Functional regulation of $Ca_V1.2$ by $Ca_V\alpha2\delta1$ requires direct interaction between the two proteins (30). Surface mapping of the 3D structure obtained with the homologous skeletal muscle $Ca_V1.1$ suggests that the two proteins share a complex interaction network (Fig. 1). Four hot spots are readily identifiable. Some residues in the extracellular loops IS1S2, IS5S6, and IIS5S6 of $Ca_V1.1$ are located within atomic distance of residues in the VWA structural domain of $Ca_V\alpha2\delta1$, whereas residues in IIIS5S6 of $Ca_V1.1$ are closer to residues in the cache1 domain of $Ca_V\alpha2\delta1$. From the close examination of the 3D structure, any or all of these interfaces could be involved in the functional modulation of Ca^{2+} currents. Functional modulation of the activation gating and increase in the peak current density could arise from the low- or moderate-affinity binding to require interaction with one or more of these interfaces such that $Ca_V\alpha2\delta1$ could alternatively associate and dissociate from $Ca_V\beta$-bound $Ca_V1.2$ proteins (31). To determine whether any or all of these extracellular loops confer functional interaction, we evaluated the functional impact of inserting an HA tag from the human influenza virus, in extracellular domains of $Ca_V1.2$. The HA tag was inserted after Ser-182 in IS1S2 ($Ca_V1.2$–HA Ser-182), after Glu-331 in IS5S6 ($Ca_V1.2$–HA Glu-331), and after Asp-710 in IIS5S6 ($Ca_V1.2$–HA Asp-710). All these constructs were translated at the expected molecular mass and expressed at the cell surface as confirmed by a flow cytometry assay (results not shown) (25, 27, 32).

Whole-cell currents were recorded after recombinant expression of HA-tagged $Ca_V1.2$ constructs with mCherry–$Ca_V\alpha2\delta1$ wild-type (WT) or alternatively with mCherry–$Ca_V\alpha2\delta1$–HA in stable $Ca_V\beta3$ cells (Fig. 2*A*) (25, 27, 32). In all cases, co-expression of the complete set of subunits yielded high-voltage-activated Ca^{2+} currents. Co-expression of $Ca_V1.2$ WT with the mCherry–$Ca_V\alpha2\delta1$ WT construct enhanced whole-cell peak current densities by ≈7–10-fold from −2.5 ±

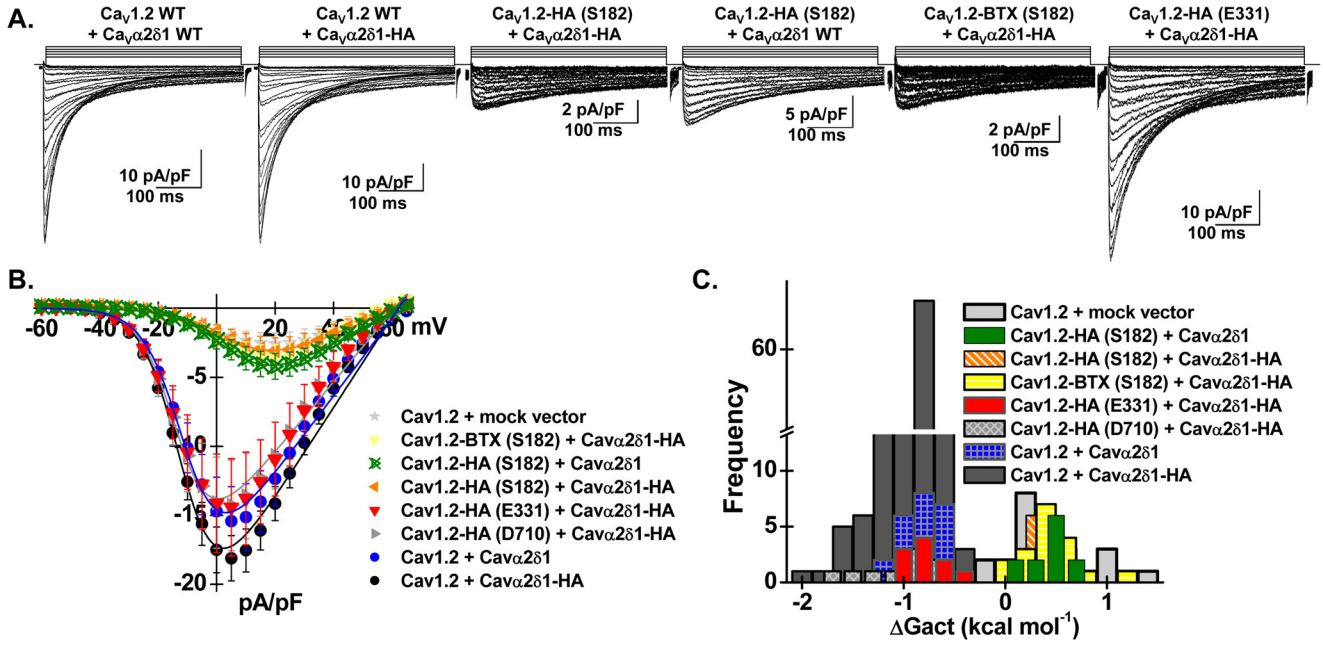

Figure 2. Inserting epitopes within the first extracellular loop of $Ca_V1.2$ prevents functional modulation of whole-cell current by $Ca_V\alpha2\delta1$. Stable recombinant HEKT cells expressing $Ca_V\beta3$ were transiently transfected with pmCherry–$Ca_V\alpha2\delta1$–HA (or pmCherry–$Ca_V\alpha2\delta1$ WT) and pCMV–$Ca_V1.2$ WT or mutants as indicated over each current trace. In all cases, $Ca_V\alpha2\delta1$ was tagged in the C terminus by an mCherry epitope. The epitopes HA or BTX were inserted after the identified residues without altering the primary sequence on each side of the insertion site. *A,* representative whole-cell Ca^{2+} current traces obtained after recombinant expression of $Ca_V1.2$ WT + $Ca_V\alpha2\delta1$ WT, $Ca_V1.2$ WT + $Ca_V\alpha2\delta1$–HA, $Ca_V1.2$-HA (Ser-182) + $Ca_V\alpha2\delta1$ WT, $Ca_V1.2$–BTX (Ser-182) + $Ca_V\alpha2\delta1$–HA, and $Ca_V1.2$–HA (Glu-331) + $Ca_V\alpha2\delta1$–HA (from *left to right*). $Ca_V1.2$ currents were modulated to the same extent in the presence of mCherry–$Ca_V\alpha2\delta1$–HA or mCherry–$Ca_V\alpha2\delta1$. Furthermore, similar results were obtained with $Ca_V1.2$–HA (Glu-331). Currents were recorded in the presence of 2 mM Ca^{2+} from a holding potential of −100 mV. Time scale is 100 ms throughout. The current density scale ranged from 2 to 10 pA/pF, as indicated. *B,* averaged current-voltage relationships. The absolute peak current densities measured with mCherry–$Ca_V\alpha2\delta1$–HA varied from −4 to −46 pA/pF over the 12-month recording period with a mean of −18 ± 1 pA/pF (n = 243). Averaged peak current densities obtained with the mock mCherry vector are shown. Co-expression with $Ca_V\alpha2\delta1$ left-shifted the voltage dependence of activation of $Ca_V1.2$ WT/$Ca_V\beta3$ from $E_{0.5,\,act}$ = +8 ± 2 mV (n = 25) to $E_{0.5,\,act}$ = −8.3 ± 0.2 mV (n = 243) for $Ca_V1.2$ WT/$Ca_V\beta3$ with mCherry–$Ca_V\alpha2\delta1$–HA. Statistical analyses were performed with a one-way ANOVA test: *, $p < 0.01$, and **, $p < 0.001$, against the mock vector. See Table 1 for details. *C,* distribution of the free energies of activation. The free energies of activation (ΔG_{act}) measured in the presence of the mock vector and in the presence of mCherry–$Ca_V\alpha2\delta1$–HA are centered at 0.5 ± 0.1 and −0.78 ± 0.03 kcal mol^{-1}, respectively. The distribution of the ΔG_{act} values for the following combinations $Ca_V1.2$–HA (Ser-182) with $Ca_V\alpha2\delta1$–HA, $Ca_V1.2$-HA (Ser-182) with $Ca_V\alpha2\delta1$ WT, and $Ca_V1.2$–BTX (Ser-182) with $Ca_V\alpha2\delta1$–HA overlapped with the ΔG_{act} values measured in the presence of the mock vector (no $Ca_V\alpha2\delta1$).

0.5 pA/pF (n = 25) (mock vector) to −15 ± 2 pA/pF (n = 23) in the presence of 2 mM Ca^{2+} (data not shown). Similar peak current densities of −18 ± 1 pA/pF (n = 243) were observed after co-expression with mCherry–$Ca_V\alpha2\delta1$–HA (Fig. 2*B* and Table 1). The increase in peak current density was associated with a ≈ −20-mV leftward shift in the activation potential of $Ca_V1.2$ (Fig. 2*C*) (25, 27). Co-expression of mCherry–$Ca_V\alpha2\delta1$–HA with $Ca_V1.2$–HA (Glu-331) or $Ca_V1.2$–HA (Asp-710) yielded similar results with activation and inactivation kinetics not significantly different from that recorded for $Ca_V1.2$ WT. The results obtained with $Ca_V1.2$–HA (Asp-710) were reported before (25). In contrast, introduction of the HA epitope or the bungarotoxin (BTX) epitope "WRYYESSLEPYPD" (33) after Ser-182 impaired the stimulation of whole-cell $Ca_V1.2$ currents by mCherry–$Ca_V\alpha2\delta1$ WT and mCherry–$Ca_V\alpha2\delta1$–HA as well as the hyperpolarizing shift in the activation potential. The patch-clamp data suggest that the modification of the primary sequence in the first extracellular loop IS1S2 in $Ca_V1.2$ disrupts the interaction with $Ca_V\alpha2\delta1$. To evaluate whether the insertion of the HA epitope disturbed the physical interaction between the two proteins, co-immunoprecipitation assays were carried out using c-Myc-tagged $Ca_V\beta3$ on anti-c-Myc-coated beads as bait (Fig. 3) (30). These assays were carried out with the same quantity of total proteins after solubilization of full-length proteins with the non-ionic detergent digitonin, thus minimizing as much as possible the alterations in the complex network of interactions between the three proteins (20).

The three proteins ($Ca_V1.2$, $Ca_V\alpha2\delta1$, and $Ca_V\beta3$) were detected at the expected molecular mass in the total cell lysates ("input lanes") when either $Ca_V1.2$ WT, $Ca_V1.2$–HA (Ser-182), $Ca_V1.2$–HA (Glu-331), or $Ca_V1.2$–HA (Asp-710) was co-expressed with $Ca_V\beta3$ and mCherry–$Ca_V\alpha2\delta1$–HA (Fig. 3*A*). Disruptions of the extracellular loops in $Ca_V1.2$ did not impair the strong interaction with $Ca_V\beta3$, and immunoblotting of the proteins bound to the beads revealed robust signals for $Ca_V1.2$ even for $Ca_V1.2$–HA (Ser-182) (Fig. 3*B*). However, the signal for $Ca_V\alpha2\delta1$ that remained hooked onto the heteromeric complex was significantly weaker in the lysates prepared with $Ca_V1.2$–HA (Ser-182) than with any other $Ca_V1.2$ construct even after longer exposure times or after doubling the quantity of proteins loaded onto the anti-c-Myc-coated beads (data not shown). $Ca_V1.2$–HA (Ser-182) was nonetheless clearly present in the flow-through (Fig. 3*C*) fraction. Altogether, these data indicate that disrupting the first extracellular loop IS1S2 in $Ca_V1.2$ prevents the functional interaction with $Ca_V\alpha2\delta1$ and suggest that the IS1S2 extracellular loop contains the elements that are important for carrying the physical interaction between the two proteins.

Table 1

Biophysical properties of $Ca_V1.2$ mutants

$Ca_V1.2$ WT or mutant was co-expressed with $Ca_V\beta3$ and either pmCherry–mock vector or pmCherry–$Ca_V\alpha2\delta1$–HA WT or mutants using a 4:4:4 μg ratio. Biophysical parameters were measured in the presence of 2 mM Ca^{2+} as described elsewhere (25, 27). Activation properties ($E_{0.5,\,act}$ and ΔG_{act}) were estimated from the mean I–V relationships and fitted to a Boltzmann equation. Null-current cells outnumbered the cells with inward currents for $Ca_V1.2$ D181R (12 null cells) and D181G (8 null cells). The data are shown as the mean ± S.E. of the number of cells (1 cell per experiment), and the total number of experiments carried over several months appears in parentheses. Statistical analysis was carried out against the values obtained in the presence of the mock pmCherry–N1 vector. NE means: no inward current;*, $p < 0.01$;**, $p < 0.001$.

$Ca_V1.2$ WT or mutants with $Ca_V\beta3$ and mCherry–$Ca_V\alpha2\delta1$–HA	Electrophysiological properties in 2 mM Ca^{2+}		
	Peak current density	$E_{0.5,\,act}$	ΔG_{act}
	pA/pF	*mV*	*kcal mol^{-1}*
mCherry mock vector	−2.5 ± 0.3 (25)	+8 ± 2	+0.5 ± 0.1
$Ca_V1.2$ WT	−18 ± 1 (243)**	−8.3 ± 0.2**	−0.78 ± 0.03**
$Ca_V1.2$-BTX (Ser-182)	−2 ± 1 (18)	+6 ± 1	+0.4 ± 0.1
$Ca_V1.2$-HA (Ser-182)	−5 ± 2 (10)	+7 ± 1	+0.5 ± 0.1
$Ca_V1.2$-HA (Glu-331)	−17 ± 4 (10)**	−8.8 ± 0.5**	−0.8 ± 0.1**
$Ca_V1.2$-HA (Asp-710)	−16 ± 2 (19)**	−8.8 ± 0.3**	−0.80 ± 0.04**
$Ca_V1.2$ E179G	−27 ± 2 (8)**	−11 ± 1**	−1 ± 0.1**
$Ca_V1.2$ E179A	−21 ± 3 (16)**	−5 ± 2**	−0.5 ± 0.1**
$Ca_V1.2$ E179I	−20 ± 3 (9)**	−7 ± 1**	−0.6 ± 0.1**
$Ca_V1.2$ E179R	−16 ± 3 (13)**	−6 ± 1**	−0.6 ± 0.1**
$Ca_V1.2$ D180G	−18 ± 2 (18)**	−2 ± 1*	−0.04 ± 0.08*
$Ca_V1.2$ D180I	−8 ± 1 (12)**	+3 ± 1	+0.24 ± 0.07
$Ca_V1.2$ D180A	−9 ± 1 (14)**	+3 ± 1	+0.2 ± 0.1
$Ca_V1.2$ D180E	−18 ± 3 (15)**	−3 ± 1*	−0.2 ± 0.1*
$Ca_V1.2$ D181G	−3 ± 2 (3)	+7 ± 4	+0.4 ± 0.3
$Ca_V1.2$ D181A	−4 ± 1 (8)**	+11 ± 6	+0.4 ± 0.2
$Ca_V1.2$ D181R	−1 ± 1 (2)	+6 ± 1	+ 0.4 ± 0.1
$Ca_V1.2$ D181E	−14 ± 3 (14)**	−4 ± 1*	−0.2 ± 0.1*
$Ca_V1.2$ D180E/D181E	−24 ± 8 (8)**	+5 ± 2	+0.3 ± 0.2
$Ca_V1.2$ S182G	−9 ± 2 (20)**	−7 ± 1**	−0.5 ± 0.1**
$Ca_V1.2$ S182A	−23 ± 7 (9)**	−8 ± 2**	−0.8 ± 0.2**
$Ca_V1.2$ S182R	−23 ± 7 (9)**	−7 ± 2**	−0.6 ± 0.1**
$Ca_V1.2$ N183G	−11 ± 2 (9)**	−7 ± 2**	−0.7 ± 0.1**
$Ca_V1.2$ N183A	−24 ± 6 (7)**	−11 ± 1**	−1 ± 0.1**
$Ca_V1.2$ N183R	−13 ± 3 (7)**	−6 ± 1**	−0.5 ± 0.1**
$Ca_V1.2$ N183Q	−7 ± 1 (7)**	−3 ± 2*	−0.3 ± 0.1*
$Ca_V1.2$ A184G	−28 ± 7 (9)**	−11 ± 1**	−1.2 ± 0.2**
$Ca_V1.2$ A184D	−22 ± 4 (9)**	−7 ± 2**	−0.8 ± 0.2**
$Ca_V1.2$ A184R	−12 ± 3 (17)**	−7 ± 1**	−0.6 ± 0.1**
$Ca_V1.2$ S957G	−26 ± 4 (6)**	−12 ± 1**	−1.3 ± 0.2**
$Ca_V1.2$ K1100A	−19 ± 4 (9)**	−9 ± 1**	−0.9 ± 0.1**
$Ca_V1.2$ K1100A + $Ca_V\alpha2\delta1$–HA E174A	−14 ± 4 (9)**	−7 ± 1**	−0.6 ± 0.1**
$Ca_V1.2$ I1104G	−21 ± 5 (10)**	−12 ± 2**	−1.1 ± 0.2**
$Ca_V1.2$ G1109A	−14 ± 4 (10)**	−7 ± 1**	−0.7 ± 0.2**
$Ca_V1.2$ H1113G	−26 ± 7 (8)**	−8 ± 2	−0.8 ± 0.2
$Ca_V1.2$ R1119A	−12 ± 2 (31)**	−10 ± 1**	−0.9 ± 0.1**
$Ca_V1.2$ R1119A + $Ca_V\alpha2\delta1$–HA D171A	−10 ± 2 (9)**	−8 ± 1**	−0.7 ± 0.1**

Cluster of negatively charged residues is conserved in IS1S2 of $Ca_V1.2$

The insertion of a 9-residue epitope after Ser-182 in the 17-residue IS1S2 extracellular loop prevented the optimal interaction with $Ca_V\alpha2\delta1$ by directly modifying the interaction site or indirectly from a nonspecific alteration of the secondary structure that was propagated to the actual interaction site. To narrow down the residues from $Ca_V1.2$ that are potentially interacting with $Ca_V\alpha2\delta1$, we run the bioinformatics tool PDBePISA (34) (http://www.ebi.ac.uk/pdbe/pisa/)[4] using the molecular coordinates 5GJV.PDB of the whole-$Ca_V1.1$ channel complex (69% residues are conserved with $Ca_V1.1$ being shorter in the N and the C termini). This led to the identification of Glu-76, Asp-78, and Ser-81 in $Ca_V1.1$ as likely candidates to form salt bridges with residues in the VWA domain of $Ca_V\alpha2\delta1$. This first level of analysis suggests that the equivalent residues in the IS1S2 loop of $Ca_V1.2$ could interact with Gly-262 and Ser-263 in $Ca_V\alpha2\delta1$. To refine the structural predictions, a 3D model of the 146-residue region spanning from IS1 to IS4 in the rabbit $Ca_V1.2$ was built using the molecular coordinates of $Ca_V1.1$ (Fig. 4). A stretch of four residues ^{74}PEDD^{77} in IS1S2 of $Ca_V1.1$ is strictly conserved and is equivalent to ^{178}PEDD^{181} in $Ca_V1.2$. Ser-81 in $Ca_V1.1$ corresponds to Ala-184 in $Ca_V1.2$. The modeled interface suggests the region ^{179}EDD^{181} in IS1S2 of $Ca_V1.2$ lies within atomic distance (<5 Å) of many residues in the rat $Ca_V\alpha2\delta1$. In particular, $Ca_V1.2$ Asp-181 arises as the most likely partner for residues Gly-262 and Ser-263 in $Ca_V\alpha2\delta1$.

$Ca_V1.2$ Asp-181 in IS1S2 anchors the physical interaction with $Ca_V\alpha2\delta1$

Because any of the three negatively charged residues could potentially interact with $Ca_V\alpha2\delta1$, co-immunoprecipitation assays were carried out with single $Ca_V1.2$ mutants E179A, D180A, and D181A to identify the role of each amino acid (Fig. 5, *A*–*C*). Again, all three proteins were detected at the expected molecular mass in the input lanes prepared from the total cell lysates. Immunoblotting of the proteins eluted from the c-Myc-coated beads revealed strong signals for $Ca_V1.2$ under all conditions even for $Ca_V1.2$ D181A. The signal for $Ca_V\alpha2\delta1$ was easily detected in the presence of $Ca_V1.2$ WT, $Ca_V1.2$ E179A,

[4] Please note that the JBC is not responsible for the long-term archiving and maintenance of this site or any other third party hosted site.

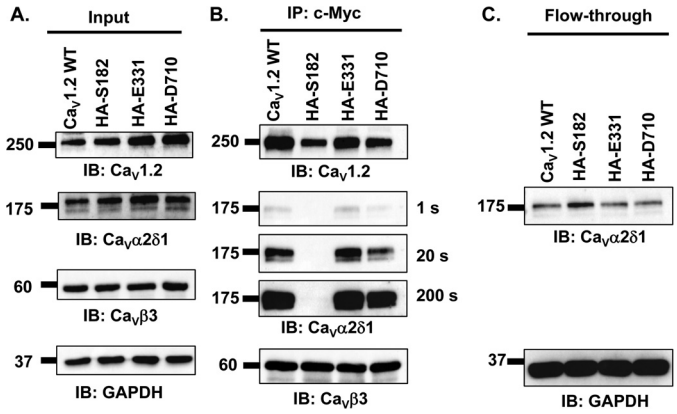

Figure 3. Epitope insertion in the first extracellular loop of $Ca_V1.2$ impairs the co-immunoprecipitation of $Ca_V\alpha2\delta1$ with $Ca_V1.2$/$Ca_V\beta3$ proteins. HEKT cells were transiently transfected with pmCherry–$Ca_V\alpha2\delta1$–HA and pCMV–$Ca_V\beta3$– c-Myc and either pCMV–$Ca_V1.2$ WT, pCMV–$Ca_V1.2$–HA (Ser-182), pCMV–$Ca_V1.2$–HA (Glu-331), or pCMV–$Ca_V1.2$–HA (Asp-710). Cell lysates were immunoprecipitated (*IP*) overnight with anti-c-Myc magnetic beads to capture $Ca_V\beta3$, eluted in a Laemmli buffer, and fractionated by SDS-PAGE using 8% gels. *A,* immunoblotting was carried out on total proteins (20 μg) collected from the cell lysates for each of the three proteins ($Ca_V1.2$, $Ca_V\alpha2\delta1$, and $Ca_V\beta3$) before the immunoprecipitation assay (*Input*) to confirm that each protein was translated at the expected molecular mass. Each experimental condition is identified by the specific $Ca_V1.2$ construct. The signal for the housekeeping protein GAPDH is shown below each blot. *B,* immunoblotting (*IB*) was carried out after eluting the protein complexes from the anti-c-Myc beads with anti-$Ca_V1.2$, anti-$Ca_V\alpha2\delta1$, and anti-$Ca_V\beta3$ antibodies (from *top to bottom*, as indicated). Images for $Ca_V\alpha2\delta1$ were captured after short (1 s) or long exposure times (20 and 200 s). $Ca_V\beta3$ and $Ca_V1.2$ proteins migrated at 60 and 250 kDa, respectively. All $Ca_V\alpha2\delta1$ proteins migrated at ≈175 kDa, which is consistent with the molecular mass of the mCherry–$Ca_V\alpha2\delta1$–HA in previous studies (30). All immunoblots were carried out in parallel under the same transfection and extraction conditions. *C,* proteins that did not bind to the antibody-bead complex (referred to as the *flow-through* fraction) were collected, diluted in a Laemmli buffer, and fractionated by SDS-PAGE using an 8% gel and revealed with the anti-$Ca_V\alpha2\delta1$. As seen, mCherry–$Ca_V\alpha2\delta1$–HA is present in the flow-through fraction at the expected molecular mass (175 kDa) confirming that the proteins were appropriately translated and were present in the preparation in detectable quantities throughout. These experiments were carried out three times with the mutants and 10 times for the WT construct over a period of 5 months and yielded qualitatively similar results.

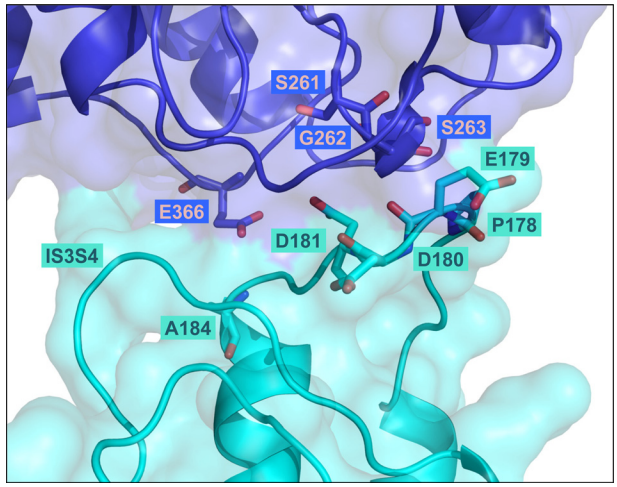

Figure 4. Three-dimensional model of the extracellular loops of the rabbit $Ca_V1.2$ in complex with the VWA domain of the rat $Ca_V\alpha2\delta1$ protein. The 3D model of the region spanning the first transmembrane helix S1 to the fourth transmembrane helix S4 in the first repeat in $Ca_V1.2$ (IS1S4) is shown in *cyan,* and the VWA domain of $Ca_V\alpha2\delta1$ is shown in *deep blue*. Residues Pro-178, Glu-179, Asp-180, Asp-181, and Ala-184 of $Ca_V1.2$ and residues Ser-261, Gly-262, Ser-263, and Glu-366 in $Ca_V\alpha2\delta1$ (three of the five residues in the MIDAS) are shown in *stick* representation with oxygen and nitrogen atoms colored in *red* and in *blue*, respectively. The model does not predict strong electrostatic interactions between $Ca_V1.2$ Asp-180 and residues in $Ca_V\alpha2\delta1$. Intramolecular interactions with residues in the extracellular IS3S4 loop are not ruled out. $Ca_V1.2$ Asp-181 appears to be appropriately oriented to form electrostatic interactions with Gly-262 and Ser-263 in $Ca_V\alpha2\delta1$. Modeling was achieved with Modeler 9.17. The figure was produced using PyMOL.

and $Ca_V1.2$ D180A. However, $Ca_V\alpha2\delta1$ could only be detected after a 200-s exposure when co-expressed with $Ca_V1.2$ D181A. These results were repeated even after doubling the quantity of $Ca_V1.2$ D181A protein as the starting material (results not shown). The protein interaction appeared thus to be considerably weakened by the mutation in $Ca_V1.2$. The properties of the side chain at position Asp-181 in $Ca_V1.2$ were further explored with a conservative substitution with a negatively charged glutamate (109 Å^3) (35). The latter is expected to cause minimal changes in steric hindrance with the addition of a single $-CH_2$ group (Δ volume ≈17–18 Å^3). As seen, all three proteins were detected at the expected molecular mass in the input lanes prepared from the total cell lysates under experimental conditions where $Ca_V1.2$ WT, $Ca_V1.2$ D180A, $Ca_V1.2$ D180E, $Ca_V1.2$ D181A, and $Ca_V1.2$ D181E were co-expressed with $Ca_V\beta3$ and mCherry–$Ca_V\alpha2\delta1$–HA (Fig. 5*D*). Immunoblotting of the proteins bound to the anti-c-Myc-coated beads revealed strong signals for the anti-$Ca_V1.2$ under all conditions indicating that all $Ca_V1.2$ proteins (WT and mutants) were hooked onto the $Ca_V\beta3$ beads. $Ca_V\alpha2\delta1$ was found to hang onto $Ca_V1.2$ WT, $Ca_V1.2$ D180A, and $Ca_V1.2$ D181E proteins as illustrated with bands of similar intensity detected after 1-s exposure (Fig. 5*E*). Again, $Ca_V\alpha2\delta1$ did not bind to the c-Myc–$Ca_V\beta3$–$Ca_V1.2$ D181A complex with the same intensity and could only be detected after a 200-s exposure. Note that the interaction between the two proteins was slightly decreased with $Ca_V1.2$ D181E despite the conservation of the negative charge, and the $Ca_V\alpha2\delta1$ signal could only be revealed after a 20-s exposure. The unbound fraction was collected, and immunoblotting confirmed that $Ca_V\alpha2\delta1$ was not in rate-limiting quantity. These results confirm that a negatively charged residue at position 181 in $Ca_V1.2$ is required to promote the interaction with $Ca_V\alpha2\delta1$ with a stronger affinity for the aspartate than the glutamate residue.

$Ca_V\alpha2\delta1$-mediated up-regulation of whole-cell currents is prevented by mutations of $Ca_V1.2$ Asp-181

The functional importance of the negatively charged side chain in conferring this interaction was confirmed in patch-clamp experiments performed with $Ca_V1.2$ mutants. Substitutions were carried out at position 181 with glycine (48 Å^3), hydrophobic alanine (67 Å^3), and arginine (148 Å^3) residues (35). In the presence of $Ca_V\alpha2\delta1$, Asp-181 mutants (D181G, D181A, and D181R) produced voltage-activated inward Ca^{2+} current currents that were indistinguishable from currents produced with $Ca_V1.2$ WT in the absence of $Ca_V\alpha2\delta1$ (Fig. 6, *A–C*, and Table 1). The near-absence of voltage-activated currents with these mutants was observed despite their cell-surface expression (Fig. 6*D*). In contrast, whole-cell currents produced by $Ca_V1.2$ D181E were up-regulated by $Ca_V\alpha2\delta1$ indicating that the functional modulation requires a negative side chain at this position. Nonetheless, the activation of $Ca_V1.2$ D181E

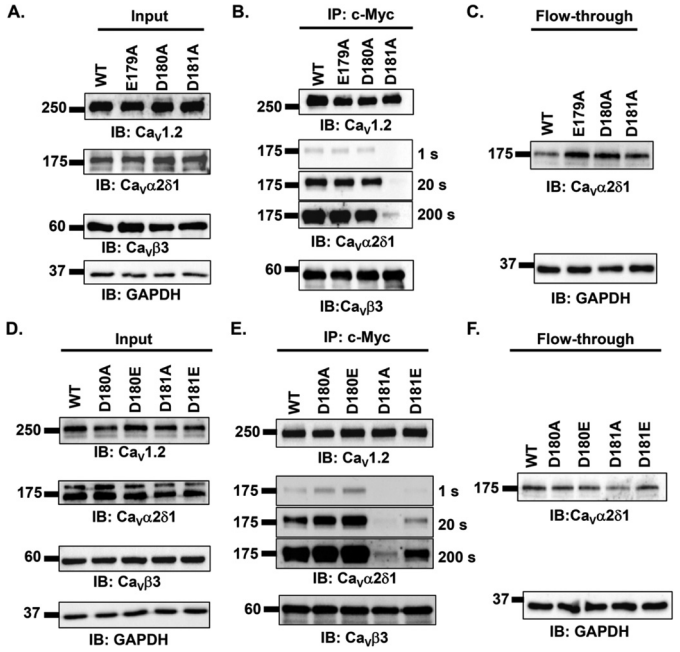

Figure 5. Mutations of the aspartate residue at position 181 impair the co-immunoprecipitation of $Ca_V\alpha2\delta1$ with $Ca_V1.2$/$Ca_V\beta3$ proteins. *A–C,* HEKT cells were transiently transfected with pmCherry–$Ca_V\alpha2\delta1$–HA and pCMV–$Ca_V\beta3$– c-Myc and either pCMV–$Ca_V1.2$ WT, pCMV–$Ca_V1.2$ E179A, pCMV–$Ca_V1.2$ D180A, or pCMV–$Ca_V1.2$ D181A. Cell lysates were immunoprecipitated (*IP*) overnight with anti-c-Myc magnetic beads to capture $Ca_V\beta3$, eluted in a Laemmli buffer, and fractionated by SDS-PAGE using 8% gels. *A,* immunoblotting was carried out on total proteins (20 μg) collected from the cell lysates for each of the three proteins ($Ca_V1.2$, $Ca_V\alpha2\delta1$, and $Ca_V\beta3$) before the immunoprecipitation assay (*Input*) to confirm that each protein was translated at the expected molecular mass. Each experimental condition is identified by the specific $Ca_V1.2$ construct. The signal for the housekeeping protein GAPDH is shown *below* each blot. *B,* immunoblotting was carried out after eluting the protein complexes from the beads with anti-$Ca_V1.2$, anti-$Ca_V\alpha2\delta1$, and anti-$Ca_V\beta3$ antibodies (from *top to bottom*, as indicated). Images for $Ca_V\alpha2\delta1$ were captured after short (1 s) or longer exposure times (20 and 200 s). All immunoblots were carried out in parallel under the same transfection and extraction conditions. *C,* proteins that did not bind to the antibody-bead complex (*flow-through fraction*) were collected, diluted in a Laemmli buffer, and fractionated by SDS-PAGE using an 8% gel and revealed with the anti-$Ca_V\alpha2\delta1$. *D–F,* HEKT cells were transiently transfected with pmCherry–$Ca_V\alpha2\delta1$–HA and pCMV–$Ca_V\beta3$– c-Myc and either pCMV–$Ca_V1.2$ WT, pCMV–$Ca_V1.2$ D180A, pCMV–$Ca_V1.2$ D180E, pCMV–$Ca_V1.2$ D181A, or pCMV–$Ca_V1.2$ D181E. Cell lysates were immunoprecipitated overnight with anti-c-Myc magnetic beads to capture $Ca_V\beta3$, eluted in a Laemmli buffer, and fractionated by SDS-PAGE using 8% gels. *D,* immunoblotting was carried out on total proteins (20 μg) collected from the cell lysates for each of the three proteins ($Ca_V1.2$, $Ca_V\alpha2\delta1$, and $Ca_V\beta3$) before the immunoprecipitation assay (*Input*) to confirm that each protein was translated at the expected molecular mass. Each experimental condition is identified by the specific $Ca_V1.2$ construct. The signal for the housekeeping protein GAPDH is shown *below* each blot. *E,* immunoblotting (*IB*) was carried out with anti-$Ca_V1.2$, anti-$Ca_V\alpha2\delta1$, and anti-$Ca_V\beta3$ antibodies (from *top to bottom*, as indicated) after eluting the protein complexes from the beads. Images for $Ca_V\alpha2\delta1$ were captured after short (1 s) or longer exposure times (20 and 200 s). All immunoblots were carried out in parallel under the same transfection and extraction conditions. *F,* proteins that did not bind to the antibody-bead complex (*flow-through fraction*) were collected, diluted in a Laemmli buffer, and fractionated by SDS-PAGE using an 8% gel and revealed with the anti-$Ca_V\alpha2\delta1$. As seen, mCherry–$Ca_V\alpha2\delta1$–HA is present in the flow-through fraction at the expected molecular mass (175 kDa) confirming that the proteins were appropriately translated and were present in the preparation in detectable quantities throughout. These experiments were carried out four times with the mutants and 10 times for the WT construct over a period of 5 months and yielded reproducible results.

was slightly right-shifted when compared with $Ca_V1.2$ WT suggesting that up-regulation of whole-cell currents can be achieved without a significant modification of the activation gating.

$Ca_V1.2$ Asp-180 influences activation gating without changing peak current density

In contrast to most mutations at position 181, $Ca_V1.2$ Asp-180 mutants produced large high-voltage-activated inward Ca^{2+} currents in the presence of $Ca_V\alpha2\delta1$ (Fig. 7 and Table 1). The stimulation of peak current densities by $Ca_V\alpha2\delta1$ ranged from 3- to 7-fold with D180A ≈ D180I < D180G ≈ D180E ≈ WT. Mutations at these positions, except for D180E, activated in a range of voltages that overlapped with $Ca_V1.2$ currents obtained in the absence of $Ca_V\alpha2\delta1$. The change in the activation potential could not be solely mediated by a change in the net electrostatic potential. Although $Ca_V1.2$ D180A and D180I are likely to alter the net negative charges at the water-accessible interface and to decrease the local Ca^{2+} concentration at the mouth of the channel pore, this effect should result in whole-cell currents being activated at more, not less, negative voltages (36). Furthermore, both $Ca_V1.2$ D180E and D181E activated at slightly more positive voltages than $Ca_V1.2$ WT despite the conservation of the net negative charge at the site, and this effect was also observed with the double mutant $Ca_V1.2$ D180E/D181E (Table 1). These observations demonstrate that physical interaction between the two proteins, as probed by the co-immunoprecipitation studies, is essential for the up-regulation of whole-cell currents. Nonetheless, a negatively aspartate-charged residue is needed at position 180 to promote the $Ca_V\alpha2\delta1$-induced negative shift in the activation of $Ca_V1.2$.

Mutations at adjacent sites confirmed that Asp residues in the IS1S2 play a unique role in the interaction with $Ca_V\alpha2\delta1$. Whole-cell currents produced by $Ca_V1.2$ single mutants at neighboring positions 179 and 182–184 were up-regulated by $Ca_V\alpha2\delta1$ and activated at potentials generally associated with $Ca_V1.2$ WT (Table 1). The results obtained with $Ca_V1.2$ Glu-179 mutants (especially E179R) do not support a significant contribution of this residue in establishing an essential interaction with $Ca_V\alpha2\delta1$.

Arg-1119 in IIIS5S6 of $Ca_V1.2$ contributes modestly to the functional interaction with $Ca_V\alpha2\delta1$

In addition to the IS1S2 loop, bioinformatics analysis based upon the 5GJV.PDB structure predicted interaction between Arg-969 and Arg-988 in the IIIS5S6 of $Ca_V1.1$ and Asp-173 and Glu-176 in the VWA domain of $Ca_V\alpha2\delta1$. The reconstructed interface built from the 3D models of IIIS5S6 in $Ca_V1.2$ and $Ca_V\alpha2\delta1$ identifies two positively charged residues in $Ca_V1.2$ Arg-1119 and Lys-1100 that could form hydrogen bonds with $Ca_V\alpha2\delta1$ Asp-171 and Glu-174, respectively (Fig. 8*A*). Within the limits of the 3D model, $Ca_V1.2$ Arg-1119 and $Ca_V\alpha2\delta1$ Asp-171 residues emerge as the most plausible pair to enable protein interaction. Co-immunoprecipitation assays carried out with the single $Ca_V1.2$ mutants suggest that Arg-1119 may be involved in the interaction between the two proteins (Fig. 8, *B–D*). Under conditions where $Ca_V1.2$ WT, R1119A, and K1100A were well-expressed (Fig. 8*B*), the signal for anti-$Ca_V\alpha2\delta1$ probed after co-immunoprecipation was slightly reduced for $Ca_V1.2$ R1119A.

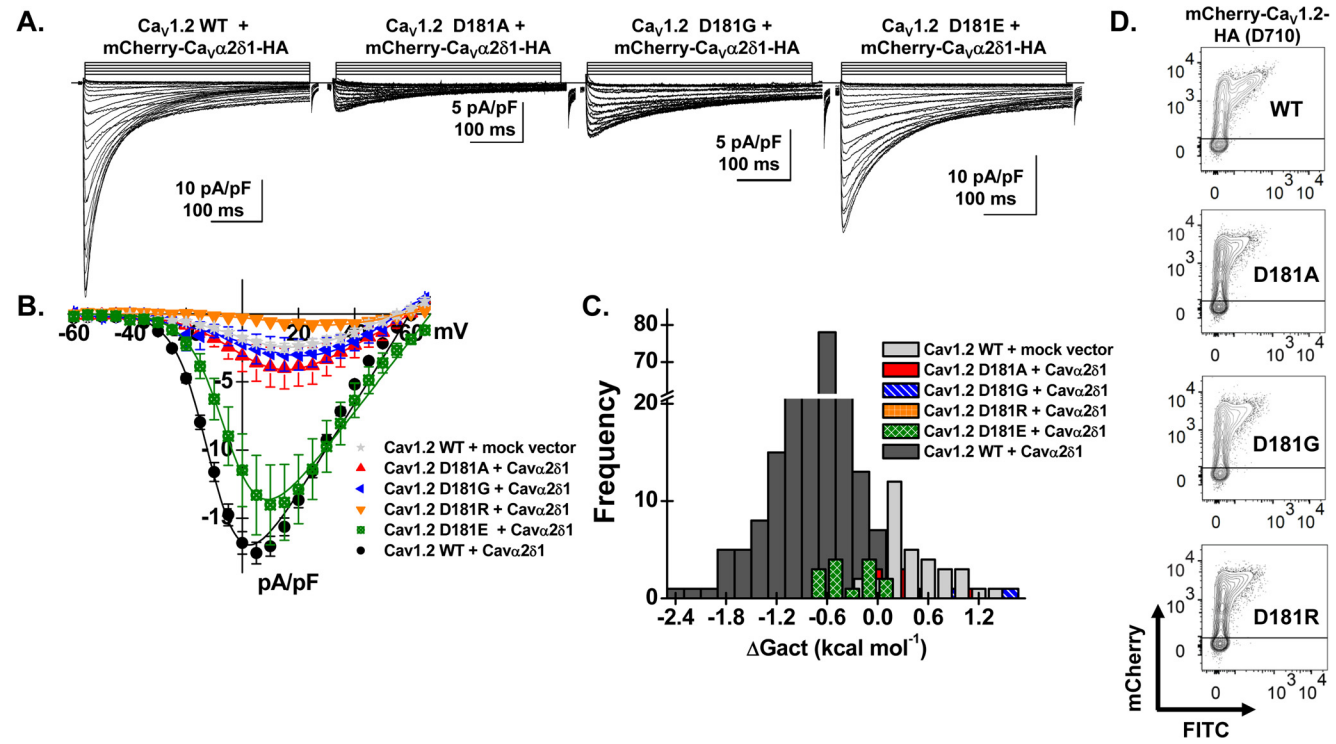

Figure 6. Mutations at Asp-181 prevent up-regulation of $Ca_V1.2$ currents. HEKT cells were transiently transfected with pCMV–Ca$_V\beta3$ and pmCherry–Ca$_V\alpha2\delta1$–HA with the Ca$_V$1.2 constructs (D181A, D181G, D181R, and D181E). *A,* whole-cell Ca^{2+} current traces were recorded in the presence of 2 mM Ca^{2+} from a holding potential of −100 mV for the constructs as identified. The current traces with the largest currents are shown for Ca$_V$1.2 constructs D181G and D181E. Time scale is 100 ms throughout. The current density scale is either 5 or 10 pA/pF as indicated. *B,* averaged current-voltage relationships. Peak current densities *versus* voltage relationships were measured for Ca$_V$1.2 WT and Ca$_V$1.2 mutants (as shown). Currents traces obtained with the empty mCherry (*mock*) vector are also shown. Ca$_V$1.2 constructs D181A, D181G, and D181R generated currents that were not significantly up-regulated by mCherry–Ca$_V\alpha2\delta1$–HA WT. Statistical analyses were performed with a one-way ANOVA test: *, $p < 0.01$, and **, $p < 0.001$ against the mock vector. See Table 1 for details. *C,* distribution of the free energies of activation. The values for the free energy of activation (ΔG_{act}) measured for Ca$_V$1.2 constructs (D181A, D181G, D181E, and D181R) overlapped with the values measured for the mock vector. *D,* representative two-dimensional plots of mCherry *versus* FITC fluorescence. The cell-surface expression of the Ca$_V$1.2 mutants was evaluated by introducing the mutation in the mCherry–Ca$_V$1.2–HA construct. The surface fluorescence was estimated from the relative intensity of the fluorescence emitted by the fluorescein isothiocyanate (FITC)-conjugated anti-HA as measured using a flow cytometry assay (10,000 intact cells). The construct allows for detection of intracellular and extracellular fluorescence using FITC-conjugated anti-HA ("*x* axis") and an anti-mCherry ("*y* axis"), respectively. The robust mCherry signal (*y* axis) confirms that the proteins were translated up to the end of the coding sequence. The cell-surface fluorescence for FITC, calculated as ΔMedFI as explained under "Experimental procedures," was slightly lower for the Ca$_V$1.2 mutants (D181A, D181G, and D181R) than for the WT construct. Nonetheless, all constructs significantly fluoresced at the cell surface supporting the view that the absence of function did not result from a complete absence of trafficking to the cell membrane. Furthermore, the ΔMedFI signal for the total protein was similar for all WT and mutant constructs demonstrating that proteins were appropriately translated, an observation also obtained from carrying out routine Western blotting.

To evaluate whether Ca$_V$1.2 Arg-1119 contributes to the functional interaction with Ca$_V\alpha2\delta1$, a series of patch-clamp experiments were conducted with Ca$_V$1.2 R1119A and/or Ca$_V\alpha2\delta1$ D171A (Fig. 9 and Table 1). As seen, the co-expression of Ca$_V$1.2 WT with Ca$_V\alpha2\delta1$ D171A did not appreciably alter the biophysical properties of Ca$_V$1.2 currents. The whole-cell currents obtained in the presence of Ca$_V$1.2 R1119A with Ca$_V\alpha2\delta1$ WT appeared to be roughly 50% lower ($p < 0.05$) than currents obtained with the two WT constructs suggesting that Ca$_V$1.2 Arg-1119 contributes to the functional interaction with Ca$_V\alpha2\delta1$. Co-expressing Ca$_V$1.2 R1119A with Ca$_V\alpha2\delta1$ D171A yielded whole-cell inward currents with biophysical properties similar to Ca$_V$1.2 R1119A with Ca$_V\alpha2\delta1$, suggesting that the interaction may not involve the side chain of Asp-171 in Ca$_V\alpha2\delta1$. Activation gating was not altered in any of these subunit combinations, and whole-cell currents were seen to activate at the same negative voltage range (Fig. 9*C*). The functional properties of the Ca$_V$1.2 K1100A and Ca$_V\alpha2\delta1$ E174A mutants were also characterized. Results indicate that substituting the charged side chain (in one or both proteins) did not significantly alter the properties of the Ca$_V$1.2 whole-cell currents (Table 1). Neighboring mutations at positions 957, 1104, 1109, and 1113 in IIIS5S6 of Ca$_V$1.2 were also without effect (Table 1). These results suggest that Arg-1119 in the IIIS5S6 loop of Ca$_V$1.2 is the residue the most likely to play a role in the functional interaction with Ca$_V\alpha2\delta1$, but its role might be more modest than Ca$_V$1.2 Asp-181.

Discussion

Negatively charged residues in the first extracellular loop control the association with $Ca_V\alpha2\delta1$

Ca$_V\alpha2\delta1$ is required to reconstitute the biophysical properties of native L-type channels in cardiomyocytes (22) and is regarded as an intrinsic subunit of Ca$_V$1.2 channels (16–20). Ca$_V\alpha2\delta1$ undergoes a complex series of co- and post-translational modifications (27, 30, 37, 38), and expression at the cell surface of the mature extracellular Ca$_V\alpha2\delta1$ protein is a prerequisite for formation of the heteromeric complex and channel modulation (30).

Ca$_V\alpha2\delta1$ produces a 5–10-fold increase in peak current density and promotes channel activation in a physiological range.

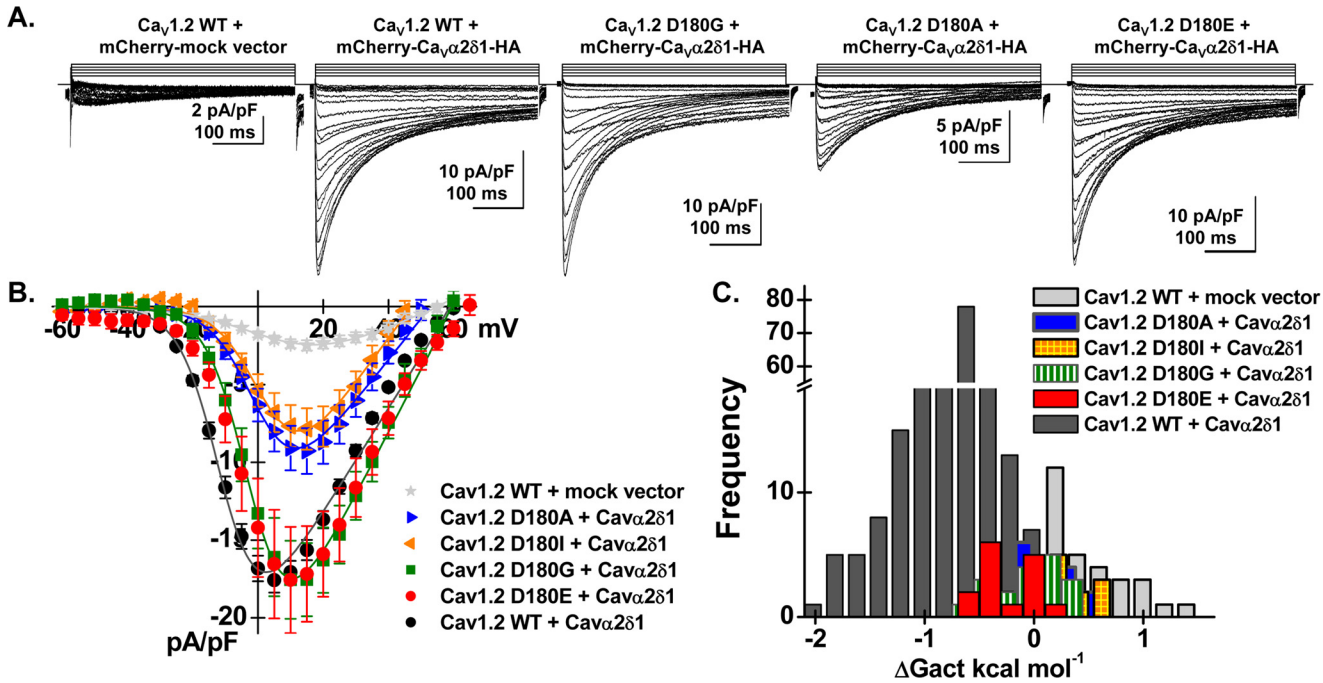

Figure 7. Asp-180 in $Ca_V1.2$ controls the $Ca_V\alpha2\delta1$-induced shift in voltage-dependent gating of $Ca_V1.2$ currents. *A,* representative whole-cell Ca^{2+} current traces obtained after the transient expression of pCMV–$Ca_V\beta3$ and pmCherry–$Ca_V\alpha2\delta1$–HA with the $Ca_V1.2$ constructs (D180I, D180A, D180G, and D180E) in HEKT cells. Note that the *leftmost* current trace was obtained in the presence of $Ca_V1.2$ WT and the mock mCherry vector. Recordings were made in the presence of 2 mM Ca^{2+} from a holding potential of −100 mV. Time scale is 100 ms throughout. The current density scale ranged from 2 to 10 pA/pF as indicated. *B,* averaged current-voltage relationships. Peak current densities *versus* voltage relationships were measured for $Ca_V1.2$ WT and $Ca_V1.2$ mutants (as shown). Averaged peak current densities obtained with the mock mCherry vector are shown in *light gray stars*. All $Ca_V1.2$ constructs (D180I, D180A, D180G, and D180E) were up-regulated by mCherry–$Ca_V\alpha2\delta$–HA albeit to variable extent. Statistical analyses were performed with a one-way ANOVA test: *, $p < 0.01$, and **, $p < 0.001$, against the mock mCherry vector. Nonetheless, the current-voltage relationships measured with the $Ca_V1.2$ mutants were clearly shifted to the right when compared with $Ca_V1.2$ WT. See Table 1 for details. *C,* distribution of the free energies of activation. The free energies of activation (ΔG_{act}) for $Ca_V1.2$ D180E, D180I, D180A, and D180G did not overlap with the values measured with $Ca_V1.2$ WT. ΔG_{act} values for $Ca_V1.2$ D180A and D180I were not significantly different from ΔG_{act} values measured for the mock vector, whereas ΔG_{act} values for $Ca_V1.2$ D180G and D180E were significantly different at $p < 0.01$.

The agonist-like properties of $Ca_V\alpha2\delta1$ are manifested by a major impact on channel gating without significant change in the protein density at the cell surface (25, 39) or in the single-channel conductance (40). $Ca_V\alpha2\delta1$ was shown to double the amount of charges moved during channel activation (41), to increase the channel mean open time in single-channel recordings (40), and to augment the effective charge moved by the voltage sensors from repeats I–III (42).

One of the most perplexing questions entails whether this functional modulation requires direct or allosteric interaction of $Ca_V\alpha2\delta1$ with the pore or the voltage sensor domains of the $Ca_V\alpha1$ subunit (31). Low-resolution cryo-EM structural data of $Ca_V1.2$ (43, 44) and more recently higher resolution of the skeletal muscle $Ca_V1.1$ channel (20, 28) have revealed that $Ca_V\alpha2\delta1$ straddles the extracellular loops in repeats I–III of the $Ca_V\alpha1$ protein with few interactions predicted between residues in repeat IV of $Ca_V1.2$ and $Ca_V\alpha2\delta1$. Herein, we used a combination of 3D modeling, co-immunoprecipitation data, and electrophysiological recordings to characterize the relative contribution of the extracellular loops in repeats I–III of $Ca_V1.2$. Introducing 9-residue epitopes after Ser-182 in IS1S2 prevented the co-immunoprecipitation of the two proteins and the functional modulation of $Ca_V1.2$ currents by $Ca_V\alpha2\delta1$. Our studies reveal that a negatively charged residue is required at position $Ca_V1.2$ Asp-181 to mediate physical interaction with $Ca_V\alpha2\delta1$ and consequently channel modulation. Substitution by glycine, hydrophobic alanine, or positively charged arginine at this position prevented protein co-immunoprecipitation and functional modulation of $Ca_V1.2$ currents, whereas the functional properties of $Ca_V1.2$ D181E were not significantly different from that observed with the WT construct. These effects were seen to be strongly position-dependent. Whole-cell currents produced by mutating the side chain at position $Ca_V1.2$ Asp-180 were up-regulated 3–7-fold by $Ca_V\alpha2\delta1$. Nonetheless, most Asp-180 mutants activated in the positive range of voltages, typically observed in the absence of $Ca_V\alpha2\delta1$. Hence, it appears that the nature of the side chain at position 180 in $Ca_V1.2$ is critical to convey the $Ca_V\alpha2\delta1$-mediated shift in the activation potential.

The contribution from extracellular loops connected to the pore region, although not being completely ruled out, can be currently qualified as being modest. Functional modulation and co-immunoprecipitation were not significantly altered when epitopes were inserted in IS5S6 and IIS5S6 of $Ca_V1.2$. Furthermore, the substitution of the positively charged Arg-1119 in IIIS5S6 of $Ca_V1.2$ decreased the peak current density but did not prevent co-immunoprecipation of the two proteins. These results suggest that there is a smaller but not negligible interaction between IIIS5S6 of $Ca_V1.2$ and $Ca_V\alpha2\delta1$ as proposed previously (42). However, we gathered little evidence for a strong role of the extracellular residues forming part of the external vestibule in the pore of repeat II (IIS5S6).

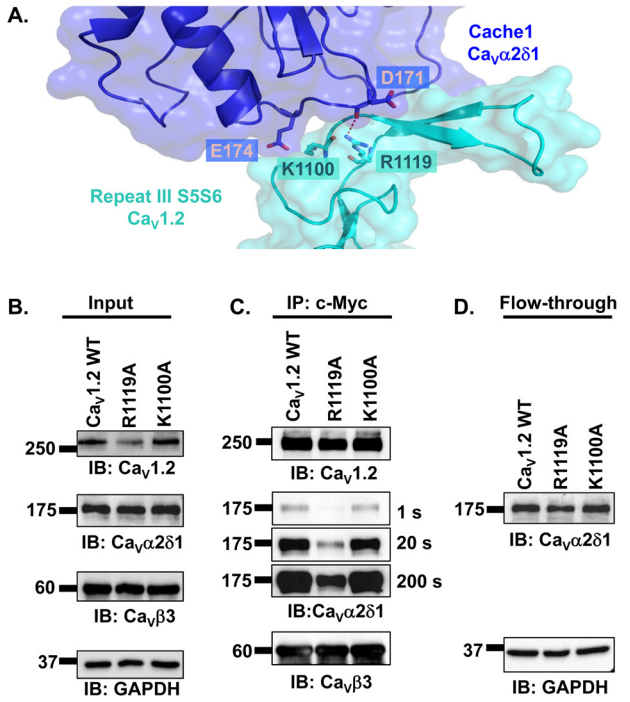

Figure 8. Extracellular loop S5S6 in repeat III has a modest impact on the interaction between $Ca_V\alpha2\delta1$ and $Ca_V1.2/Ca_V\beta3$ proteins. *A,* 3D model of IIIS5S6 in $Ca_V1.2$ (residues 1059–1204) is shown in *cyan*, and the cache1 domain (residues 104–223) in $Ca_V\alpha2\delta1$ is shown in *deep blue*. The carboxyl group on the side chain of Arg-1119 in $Ca_V1.2$ is located close enough (< 3 Å) to the main-chain atoms of Glu-171 in $Ca_V\alpha2\delta1$ to potentially contribute to the formation of hydrogen bonds. In contrast, the 3D model does not predict a favorable interaction between Lys-1100 in $Ca_V1.2$ and Glu-174 in $Ca_V\alpha2\delta1$ with a minimum distance estimated to be at 4.6 Å. Modeling was achieved with Modeler 9.17. The figure was produced using PyMOL. *B–D,* HEKT cells were transiently transfected with pmCherry–$Ca_V\alpha2\delta1$–HA WT and pCMV–$Ca_V\beta3$– c-Myc and either pCMV–$Ca_V1.2$ WT, pCMV–$Ca_V1.2$ R1119A, or pCMV–$Ca_V1.2$ K1100A. Cell lysates were immunoprecipitated overnight with anti-c-Myc magnetic beads to capture $Ca_V\beta3$, eluted in a Laemmli buffer, and fractionated by SDS-PAGE using 8% gels. *B,* immunoblotting (*IB*) was carried out on total proteins (20 μg) collected from the cell lysates for each of the three proteins ($Ca_V1.2$, $Ca_V\alpha2\delta1$, and $Ca_V\beta3$) before the immunoprecipitation assay (*Input*) to confirm that each protein was translated at the expected molecular mass. Each experimental condition is identified by the specific $Ca_V1.2$ construct. *C,* immunoblotting was carried out as detailed earlier. Images for $Ca_V\alpha2\delta1$ were captured after 1, 20, and 200 s of exposure. The signal for the anti-$Ca_V\alpha2\delta1$ was detected only after a 200-s exposure when probed in the presence of $Ca_V1.2$ R1119A/$Ca_V\beta3$. *D,* protein lysates that ran through without binding to the antibody-bead complex (*flow-through fraction*) were collected, diluted in a Laemmli buffer, and fractionated by SDS-PAGE using an 8% gel and revealed with the anti-$Ca_V\alpha2\delta1$. As seen, mCherry–$Ca_V\alpha2\delta1$–HA is present in all flow-through fractions at the expected molecular mass (175 kDa) confirming that the proteins were appropriately translated and were present in the preparation in detectable quantities throughout.

Our results are qualitatively in agreement with voltage-clamp fluorometry data obtained on $Ca_V1.2/Ca_V\beta3/Ca_V\alpha2\delta1$ channels showing that the four voltage sensors are not functionally equivalent (45). Experiments from the same group further demonstrated that $Ca_V\alpha2\delta1$ enhances the charge displacement and promotes the energetic contribution from voltage sensors in repeats I–III (42). Close examination of these data suggest that $Ca_V\alpha2\delta1$ modifies more significantly the properties of the voltage sensor in repeat II, but these differences may result from changes in the conformations of the specific $Ca_V1.2$ and $Ca_V\alpha2\delta1$ constructs. It is in fact remarkable that the dataset are such in good agreement given the intrinsically distinct experimental designs. The $Ca_V\alpha2\delta1$ construct we used was tagged with a mCherry fluorophore in its C terminus and a HA epitope in its extracellular cache2 domain, and we have modified key residues in extracellular loops of $Ca_V1.2$. Voltage-clamp fluorometry experiments were carried out with the unadulterated $Ca_V\alpha2\delta1$ protein after the covalent modification of the $Ca_V1.2$ protein modified at selected positions in the extracellular loops linking S3 and S4. Future experiments are needed to elucidate further the complex set of interactions and the complete energy landscape at the hydrophilic interface.

What is the putative mechanism responsible for the $Ca_V\alpha2\delta1$-mediated modulation of $Ca_V1.2$?

Molecular dynamics simulations of our 3D model suggest that $Ca_V1.2$ Asp-181 establishes electrostatic interactions with Ser-263 with minor contributions from the adjacent residues Ser-261 and Gly-262 in the VWA domain of $Ca_V\alpha2\delta1$. Long-range interactions contrast with the nanomolar high-affinity hydrophobic van der Waals interactions at the $Ca_V1.2/Ca_V\beta$ interface, which is anchored by a unique tryptophan residue in the pore-forming subunit (15, 21, 29) facing leucine residues in the guanylate domain of $Ca_V\beta$ (46). Polar interactions are often found at the protein interface of loosely connected protein complexes with association constants in the micromolar range (47). Although not identified in the high-resolution cryo-EM structure, it is likely possible that water molecules are present at the interface and play a role in mediating the interaction between the two proteins. The movement of water molecules would in turn increase the number of configurations that the side chains can adopt at the hydrophilic interface.

Within the precision of the cryo-EM structure and the 3D model of the extracellular loops of $Ca_V1.2$, we propose that the IS1S2 loop undergoes a conformational change prompted by the binding of $Ca_V\alpha2\delta1$, which would in turn stabilize salt bridges known to be formed between positively charged S4 residues and negatively charged residues in S2 and S3 transmembrane helices (48, 49). $Ca_V\alpha2\delta1$ could be required to stabilize the secondary structure of the extracellular IS1S2 loop around Pro-178. In this scheme, negatively charged residues Asp-180 and Asp-181 play essential roles in modifying the energy landscape. First, the interaction of Asp-181 with $Ca_V\alpha2\delta1$ could stabilize the interaction between residues forming the MIDAS that is required for the function of $Ca_V\alpha2\delta1$ (50) such that substitution of the negative charge at position 181 in $Ca_V1.2$ would destabilize MIDAS. This interpretation is congruent with molecular dynamics simulations indicating that the presence of Ca^{2+} in the MIDAS increases the strength of the non-bonded interactions between residues $Ca_V1.2$ Asp-181 and $Ca_V\alpha2\delta1$ Ser-263. In addition, the strong interactions between $Ca_V\alpha2\delta1$ and $Ca_V1.2$ Asp-181 could promote a long-lived conformation in $Ca_V1.2$ that would facilitate the intramolecular interaction of $Ca_V1.2$ Asp-180 with the external IS3S4 loop. This interaction could be propagated through water molecules, likely to be abundant at the hydrophilic interface. Alteration in the side chain at Asp-180 could thus compromise its interaction with the IS3S4 loop without perturbing significantly the physical interaction with $Ca_V\alpha2\delta1$. In turn, the interaction between Asp-180 and the IS3S4 loop could promote a conformation that

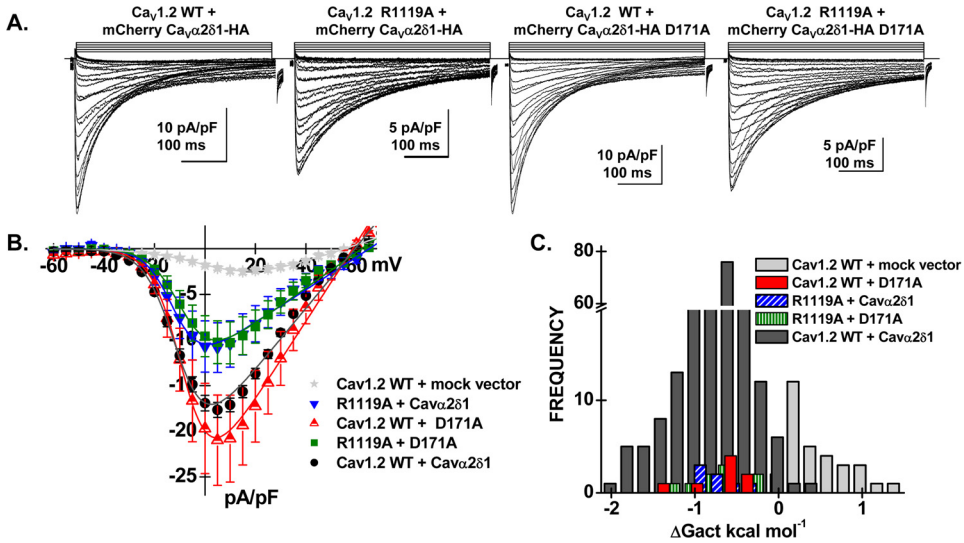

Figure 9. Double mutant analysis of charged residues in repeat III in $Ca_V1.2$. HEKT cells were transiently transfected with $Ca_V\beta3$, pCMV–$Ca_V1.2$ WT or mutant and pmCherry–$Ca_V\alpha2\delta1$–HA WT or mutant. *A,* representative whole-cell Ca^{2+} current traces were recorded in the presence of 2 mM Ca^{2+} from a holding potential of −100 mV. From *left to right*: $Ca_V1.2$ WT with mCherry–$Ca_V\alpha2\delta1$–HA WT; $Ca_V1.2$ R1119A with mCherry–$Ca_V\alpha2\delta1$–HA WT; $Ca_V1.2$ WT with mCherry–$Ca_V\alpha2\delta1$–HA D171A, and $Ca_V1.2$ R1119A with mCherry–$Ca_V\alpha2\delta1$–HA D171A. Time scale is 100 ms throughout. The current density scale is either 5 or 10 pA/pF as indicated. *B,* averaged current-voltage relationships. Peak current densities *versus* voltage relationships were measured for the WT construct and the mutants (as shown). Current traces obtained with the empty mCherry vector (mock vector) are also shown. Statistical analyses were performed with a one-way ANOVA test: *, $p < 0.01$, and **, $p < 0.001$, against the mock vector. See Table 1 for details. *C,* distribution of the free energies of activation. The values of the free energy of activation (ΔG_{act}) for all conditions were significantly different from the values measured with the mock vector.

could lock the S4 voltage sensor into the open state and thus account for the improved activation gating. More experiments are needed to confirm this model and assess its universality in regard to the modulation of high-voltage-activated Ca_V2 channels by $Ca_V\alpha2\delta1$. In the context where the molecular properties of the extracellular S3S4 loops are critical determinants of the gating properties in L-type $Ca_V1.1$ channels (49), it is also important to note that the atomic coordinates of the IS3S4 loop are missing from the 5GJV.PDB structure and were constructed *de novo* in our virtual model. At this time, we propose that $Ca_V\alpha2\delta1$ modulates $Ca_V1.2$ currents by indirectly exerting its effect on the voltage sensor domain in repeat I rather than on the pore region.

Experimental procedures

Recombinant DNA techniques

The rabbit $Ca_V1.2$ (GenBank™ X15539) and the rat $Ca_V\beta3$ (GenBank™ M88751) were subcloned in commercial vectors under the control of the CMV promoter as described elsewhere (25, 46). The coding sequence (1091 residues) of the rat brain $Ca_V\alpha2\delta1$ clone (GenBank™ NM_012919) (51) was subcloned in the pmCherry–N1 vector, and the hemagglutinin (HA) epitope (YPYDVPDYA) was inserted in the extracellular domain of $Ca_V\alpha2$ between Asp-676 and Arg-677, such that the HA epitope is accessible from the extracellular medium, and the mCherry is translated after the C terminus. This construct enables the detection of the $Ca_V\alpha2\delta1$ proteins expressed at the cell surface as described previously (27, 30, 32). Point mutations and insertions were produced with the Q5 site-directed mutagenesis kit (New England Biolabs) in the pCMV–$Ca_V1.2$ and in the pmCherry–$Ca_V\alpha2\delta1$–HA (in Fig. 9) constructs according to the manufacturer's instructions as described elsewhere (25, 27). The HA or the BTX (WRYYESSLEPYPD) epitope tags were inserted between Ser-182 and Asn-183 within the S1–S2 extracytoplasmic loop in repeat I of the $Ca_V\alpha1$ subunit of $Ca_V1.2$. The HA epitope tag was also inserted in two other sites, between Gln-331 and Glu-332 (S5–S6 loop, repeat I) and between Asp-710 and Glu-711 (S5–S6 loop, repeat II). All HA and BTX constructs were produced with the Q5 site-directed mutagenesis kit (New England Biolabs) according to the manufacturer's instructions. Briefly, large insertions (9–13 amino acids) were performed by incorporating half of the desired insertion into the 5′ ends of both desalted primers. After PCR, a kinase/ligase/DpnI enzyme mix was added to the amplified DNA for circularization and template removal before transformation into high-efficiency DH5-α-competent *Escherichia coli* (New England Biolabs). All constructs were verified by automated double-stranded sequence analysis (Genomics Platform, IRIC, Université de Montréal, Quebec, Canada).

Immunoblotting of total cell lysates from HEKT cells

Protein expression of all constructs was confirmed by Western blotting in total cell lysates but not shown herein (21, 25, 27). Briefly, HEKT cells were lysed with a RIPA buffer (150 mM NaCl, 1% IGEPAL, 0.5% sodium deoxycholate, 0.1% SDS, 50 mM Tris, pH 8.0) containing a protease inhibitor mixture including 4-(2-aminoethyl)benzenesulfonyl fluoride hydrochloride, aprotinin, bestatin, E-64, leupeptin, and 1 mM EDTA (Sigma) for 30 min at 4 °C. The cell lysates were sonicated and centrifuged at 13,000 rpm for 30 min at 4 °C. Supernatant was collected, and proteins were quantified with the Pierce BCA Protein Assay Kit (Thermo Fisher Scientific, Ottawa, Ontario, Canada). Immunoblotting was carried out with fresh lysates. Proteins were mixed with the Laemmli sample buffer in the presence of 0.4 mM 2-mercaptoethanol and electrophoresed on an 8% SDS-polyacrylamide gel alongside the Precision Plus

Protein™ dual-color standard (Bio-Rad). After electroblotting and blocking with 5% (w/v) skim milk for 30 min, the supported nitrocellulose membranes (Bio-Rad) were incubated with the appropriate antibodies. The $Ca_V1.2$ mutants were tested with the anti-$Ca_V1.2$ (Alomone, Jerusalem, Israel, 1:5000). Membranes were stripped and incubated with an anti-GAPDH as a loading control (Sigma, 1:10,000) unless stated otherwise. Signals were detected with the ECL substrate. Blots were visualized with the ChemiDoc Touch system (Bio-Rad). Molecular weights were estimated using Image Lab™ software version 5.2 (Bio-Rad) by linear regression of standard molecular weight markers.

Co-immunoprecipitation of $Ca_V1.2$ and $Ca_V\alpha2\delta1$ with $Ca_V\beta3$-c-Myc

HEKT cells were transiently transfected with pCMV–$Ca_V\beta3$-c-Myc and pCMV–$Ca_V1.2$ WT or mutants and pmCherry–$Ca_V\alpha2\delta1$–HA WT. Two days after transfection, cells were homogenized in 20 mM NaMOPS (pH 7.4), 300 mM NaCl, and 1% digitonin supplemented with protease inhibitors (Thermo Fisher Scientific). Homogenates were sonicated, incubated for 1 h at 4 °C, and centrifuged at 16,000 × *g* for 30 min. A fraction (20 μg) of the homogenates or starting material was set aside as the input fraction and was immunoblotted to confirm the presence of all three proteins of interest. Co-immunoprecipitation was carried out using 150 μl of the homogenates containing 3.8 ± 0.1 μg/μl (n = 48) of total proteins. This solution (containing 555–585 μg of total proteins) was diluted with an equal volume of 20 mM NaMOPS (pH 7.4), 300 mM NaCl (to 0.5% final concentration of digitonin) and mixed by pipetting. The 300-μl protein solution was incubated overnight with 50 μl of anti-c-Myc magnetic beads (Thermo Fisher Scientific). Beads were collected using a PureProteome magnetic rack (Millipore). The flow-through fraction containing the unbound proteins was conserved, and 15 μl of this protein solution was immunoblotted to validate the presence of $Ca_V\alpha2\delta1$ in all samples. The magnetic beads were washed three times with a buffer containing 20 mM NaMOPS (pH 7.4), 300 mM NaCl, and 0.2% digitonin. The bound proteins were eluted with 20 μl of Laemmli buffer at 95 °C for 5 min, electrophoresed on an 8% SDS-polyacrylamide gel, and transferred onto a nitrocellulose membrane. Western blotting was carried out with either anti-$Ca_V\beta3$ (Alomone, 1:10,000), anti-$Ca_V1.2$ (Alomone, 1:5000), or the anti-$Ca_V\alpha2\delta1$ (Alomone, 1:1000) with an anti-rabbit as secondary antibody (Jackson ImmunoResearch, 1:10,000).

Signals were detected with the ECL chemiluminescent substrate (Thermo Fisher Scientific), and blots were visualized with the ChemiDoc Touch system (Bio-Rad). Each series of experiments was performed a minimum of three separate times after loading the same quantity of proteins onto the beads.

Flow cytometry assays

Flow cytometry experiments were carried out to evaluate the cell-surface expression of the mCherry–$Ca_V1.2$–HA WT and mutants studied in electrophysiology. Stable $Ca_V\beta3$ cells were transiently transfected with pCMV–$Ca_V\alpha2\delta1$ WT and pmCherry–$Ca_V1.2$–HA WT or mutants where the HA epitope was inserted after Asp-710 (32). Experiments were conducted and analyzed as published before (25, 27, 30) and described in greater details elsewhere (32). Briefly, the cell-surface expression of the mCherry–$Ca_V1.2$–HA WT was detected with the FITC-conjugated mouse monoclonal anti-HA epitope tag antibody at 5 μg/ml (Sigma). To determine the total quantity of both intracellular and extracellular expression of the tagged proteins, cells were fixed and permeabilized using BD Cytofix/Cytoperm™ fixation/permeabilization solution kit (BD Biosciences). This procedure was especially important for the mutants that failed to generate significant cell-surface fluorescence as a means to confirm the accessibility of the HA epitope. Roughly 10,000 cells were counted using a FACSAria III® SORP flow cytometer (BD Biosciences). The control conditions were carried out in triplicate with each series of experiments as follows: (*a*) untransfected $Ca_V\beta3$ cells without the anti-HA FITC-conjugated antibody; (*b*) untransfected $Ca_V\beta3$ cells with the anti-HA FITC-conjugated antibody to assess the level of background staining; and (*c*) $Ca_V\beta3$ cells transfected with pCMV–$Ca_V\alpha2\delta1$ WT and pmCherry–$Ca_V1.2$–HA WT, the latter serving as a quality control of transfection. Expressing mCherry–$Ca_V1.2$ HA WT in HEKT cells produced a 1-log increase in the FITC ("*x*" axis) and a 3-log increase in mCherry fluorescence ("*y*" axis) on two-dimensional dot plots as shown in Fig. 6*D*.

Although not reported in details herein, flow cytometry data were analyzed using the FlowJo software, version 10 (TreeStar, Ashland, OR) as described (32). Relative expression of the pore-forming subunit of $Ca_V1.2$ ($Ca_V\alpha1.2$) was calculated based on Δmedian fluorescence intensity (ΔMedFI) for each fluorophore (mCherry or FITC). ΔMedFI for FITC measured in intact non-permeabilized cells was used as a relative index of the steady-state cell-surface expression of the HA-tagged $Ca_V1.2$, whereas the ΔMedFI for mCherry attested that the protein was translated until the C terminus. ΔMedFI values were normalized to the maximum value measured the same day for mCherry–$Ca_V1.2$–HA WT expressed under the same conditions. The normalized ΔMedFI values for mCherry measured for each mutant in intact and permeabilized cells were not significantly different from one another ($p > 0.1$) (data not shown) suggesting that the cell permeabilization procedure did not distort significantly the relative fluorescence readout under most conditions.

Patch-clamp experiments in HEKT cells

Whole-cell patch-clamp experiments were carried out on isolated cells after transfection in HEKT cells in the presence of the peGFP vector coding for the green fluorescence protein (GFP) (0.2 μg) as a control for transfection efficiency. Only the GFP-positive cells were patched. Electrodes were filled with a solution containing (in mM) 140 CsCl, 0.6 NaGTP, 3 MgATP, 10 EGTA, 10 HEPES and titrated to pH 7.3 with NaOH with a resistance varying between 2.8 and 3.2 megohms. Cells were bathed in a modified Earle's saline solution containing (in mM) 135 NaCl, 20 TEA-Cl, 2 $CaCl_2$, 1 $MgCl_2$, 10 HEPES and titrated to pH 7.3 with KOH. GFP-positive cells were selected for patching. On-line data acquisition was achieved with the Axopatch

200-B amplifier (Molecular Devices, Sunnyvale, CA) connected with the PClamp software Clampex 10.5 through the Digidata 1440A acquisition system (Molecular Devices) (25). A series of 450-ms voltage pulses were applied from a holding potential of −100 mV at a frequency of 0.2 Hz, from −60 to +70 mV at 5-mV intervals. Series resistance was compensated to ~85% after on-line capacitive transient cancellation. Unless stated otherwise, whole-cell currents were sampled at 5 kHz and filtered at 1 kHz. PClamp software Clampfit10.5 was used for data analysis. Mid-potential of activation values ($E_{0.5,\,act}$) was estimated from the peak I–V curves obtained for each channel composition and were reported as the mean of individual measurements ± S.E. (25, 52). The free energy of activation was calculated using the mid-activation potential shown in Equation 1,

$$\Delta G_{act} = z \cdot F \cdot E_{0.5,\,act} \quad \text{(Eq. 1)}$$

where z is the effective charge displacement during activation; and F is the Faraday constant. The r100 ratio, defined as the ratio of peak whole-cell currents remaining after a depolarizing pulse of 100 ms ($I_{100\ ms}/I_{Peak}$), was calculated for each mutant. As there was no significant change in the channel kinetics, these values were not reported herein. To assess for internal consistency, the experiments carried out with novel mutants always included a control experiment performed with pCMV–$Ca_V1.2$ WT (pCMV–$Ca_V1.2$ WT + pCMV–$Ca_V\beta3$ + pmCherry–$Ca_V\alpha2\delta1$–HA WT) thus explaining the larger sample size for $Ca_V1.2$ WT. Previous experiments confirmed that mCherry–$Ca_V\alpha2\delta1$–HA WT sustains the functional modulation of $Ca_V1.2$ currents (25). Experiments performed under the same conditions yielded peak current densities that could vary by as much as ±35% between each series of transfections. This variation appeared to be essentially linked to minor changes in the cell density at the time of transfection. Data from all experiments performed under the same conditions over a period of 15 months were pooled, and biophysical properties are reported in the Table 1. Experiments were performed at room temperature (22 °C).

3D homology modeling

The atomic coordinates of the $Ca_V\alpha1$ protein from $Ca_V1.1$ (Protein Data Bank 5GJV) were used to explore the 3D structure of $Ca_V1.2$. The rabbit $Ca_V1.1$ (1873 amino acids) and rabbit $Ca_V1.2$ (2171 amino acids) share 69.3% identity (86.3% similarity) in the 1714-residue overlap between 107 and 1806 ($Ca_V1.1$ numbering) with major differences found in the N and C termini. Attempts of modeling the four repeats of the $Ca_V\alpha1$ protein from $Ca_V1.2$ using the cryo-EM coordinates of $Ca_V1.1$ failed to yield 3D models with small root mean square deviations due in large part to the gaps in the atomic coordinates of the $Ca_V\alpha1$ protein of $Ca_V1.1$, namely for amino acids 139–161 in IS3–S4; 343–357 and 372–425 in IS6–IIS1; 669–798 in IIS6–IIIS1; 1076–1103 in IIIS6–IVS1; 1204–1229 in IVS3S4; and 1396–1671 after IVS6. The atomic coordinates of the extracellular loops IS1S4 and IIIS5S6 predicted to interact with $Ca_V\alpha2\delta1$ were used to build 3D models of these two regions.

The primary sequence between helix S1 and helix S4, in repeat I of the rabbit $Ca_V1.2$ (GenBank™ X15539), shares 69.6% identity with the same region of the rabbit $Ca_V1.1$. The primary sequence of the VWA domain of the rat $Ca_V\alpha2\delta1$ (our construct, GenBank™ NM_012919) between amino acids 249 and 439 is perfectly conserved between both species. Amino acids 135–281 in $Ca_V1.2$ and amino acids 249–439 of the rat $Ca_V\alpha2\delta1$ were simultaneously aligned to the atomic coordinates of Protein Data Bank 5GJV using the align2D algorithm in Modeler9.17 (53). Modeler 9.17 was used to generate 100 3D models, and the models with the lowest values for the molpdf parameters and discrete optimized protein energy (DOPE) score (54), as reported in the log file, were selected. The DOPE parameter is a statistical potential used to access the energy of the protein model generated through many iterations by Modeler, which produces homology models by the satisfaction of spatial restraints. The gaps of the cryo-EM structure in the extracellular loop linking helix S3 and helix S4 were filled in using PHENIX (phenix.refine) (55) and further refined using the "automatic loop refinement" tool in Modeler. Modeler was used to generate 100 3D models, and the models with the lowest values for the molpdf parameters and DOPE score (54) were selected for this study.

The 3D model of the extracellular loop between transmembrane segments 5 and 6 in repeat III (IIIS5S6) in $Ca_V1.2$ was built using Modeler9.17 (53) using a similar strategy. This 145-residue gapless stretch in $Ca_V1.2$ (residues 1059–1204) shares 74% identity with $Ca_V1.1$. The best model with the lowest value of DOPE score and an average root mean square deviation of 0.4 Å was selected. The protein/protein interfaces were reconstructed in PyMOL. The 3D model of IIIS5S6 in $Ca_V1.2$ and the 3D model of the cache1 domain (104–233) of the rat $Ca_V\alpha2\delta1$ were superimposed with the cryo-EM structure of the $Ca_V1.1$ protein complex (PDB code 5GJV). The reconstructed interface shows that residues Lys-1100 and Arg-1119 could form hydrogen bonds with Glu-174 and Asp-171, respectively, in the VWA domain of $Ca_V\alpha2\delta1$.

Molecular dynamics simulations were performed using CHARMM-CGENFF with explicit solvent water molecules. The system comprises the external loops IS1S2 and IS3S4 of $Ca_V1.2$ extending from Ala-172 to Glu-190 and Glu-243 to Val-263, respectively, plus the VWA domain of the rat $Ca_V\alpha2\delta1$ extending from Ala-249 to Ala-441. Identification of the water-exposed external loops was based on the PPM server calculations, which determine the rotational and translational positions of transmembrane and peripheral proteins in membranes using their 3D structure (PDB coordinate file) as input as seen in http://opm.phar.umich.edu/server.php[4] (57). The system was solvated in a 84.5 Å side cubic cell containing 19 938 TIP3P model water molecules. Altogether the system consisted of 63,938 atoms, including 60 K^+ and 56 Cl^- ions to ensure electroneutrality at near physiological concentrations. Cut-on and cut-off parameters needed to define non-bonded interactions were set to 10 and 12 Å, respectively, and SHAKE constraints were used to determine the lengths of bonds involving hydrogen atoms. Constraints with a force of 10 were applied to the end residues of IS1S2 of $Ca_V1.2$ (Ala-172 and Glu-190), IS3S4 (Glu-243 and Val-263), and the VWA domain (Ala-249 and Ala-441) to account for the anchoring of the IS1S2 and IS3S4 loops to their respective transmembrane segments and the

folding of the VWA domain between the cache1 and the cache2 domains. Trajectories were generated for 20 and 25 ns (in the presence and in the absence of Ca^{2+}, respectively) using a time step of 2 fs, and electrostatic and van der Waals interaction energies computed from trajectories were sampled at 0.01 ns. Molecular dynamics simulations were performed for a system at constant pressure (1 atm) and constant temperature (303 K).

Statistics

Results were expressed as mean ± S.E. Tests of significance were carried out using the unpaired ANOVA with the Tukey Test embedded in the Origin 7.0 analysis software (OriginLab Corp., Northampton, MA). Data were considered statistically significant at *, $p < 0.01$, and **, $p < 0.001$.

Author contributions—B. B. conducted and analyzed the patch-clamp experiments. J. B. was responsible for the homology modeling and carried out the co-immunoprecipitation assays. M. P. T. performed and analyzed flow-cytometry experiments. B. B. and M. P. T. produced the mutants. B. B., J. B., and M. P. T. performed standard immunoblotting assays. R. S. supervised the homology modeling and performed molecular dynamics simulations. L. P. coordinated the study, interpreted the data, and wrote the manuscript. All authors contributed to the design of the experiments, reviewed the results, and approved the final version of this manuscript.

Acknowledgments—We thank Armelle LeCampion and Dr. Jacques Thibodeau for sharing their expertise and granting us access to their flow cytometry and cell-sorting platform; we also thank Behzad Shakeri for preliminary electrophysiological experiments.

References

1. Bers, D. M. (2000) Calcium fluxes involved in control of cardiac myocyte contraction. *Circ. Res.* **87,** 275–281
2. Jaleel, N., Nakayama, H., Chen, X., Kubo, H., MacDonnell, S., Zhang, H., Berretta, R., Robbins, J., Cribbs, L., Molkentin, J. D., and Houser, S. R. (2008) Calcium influx through T- and L-type calcium channels have different effects on myocyte contractility and induce unique cardiac phenotypes. *Circ. Res.* **103,** 1109–1119
3. Gao, H., Wang, F., Wang, W., Makarewich, C. A., Zhang, H., Kubo, H., Berretta, R. M., Barr, L. A., Molkentin, J. D., and Houser, S. R. (2012) Calcium influx through L-type calcium channels and transient receptor potential channels activates pathological hypertrophy signaling. *J. Mol. Cell. Cardiol.* **53,** 657–667
4. Bannister, J. P., Bulley, S., Narayanan, D., Thomas-Gatewood, C., Luzny, P., Pachuau, J., and Jaggar, J. H. (2012) Transcriptional upregulation of $\alpha2\delta1$ elevates arterial smooth muscle cell voltage-dependent Ca^{2+} channel surface expression and cerebrovascular constriction in genetic hypertension. *Hypertension* **60,** 1006–1015
5. Yue, L., Feng, J., Gaspo, R., Li, G. R., Wang, Z., and Nattel, S. (1997) Ionic remodeling underlying action potential changes in a canine model of atrial fibrillation. *Circ. Res.* **81,** 512–525
6. Van Wagoner, D. R., Pond, A. L., Lamorgese, M., Rossie, S. S., McCarthy, P. M., and Nerbonne, J. M. (1999) Atrial L-type calcium currents and human atrial fibrillation. *Circ. Res.* **85,** 428–436
7. Aschar-Sobbi, R., Izaddoustdar, F., Korogyi, A. S., Wang, Q., Farman, G. P., Yang, F., Yang, W., Dorian, D., Simpson, J. A., Tuomi, J. M., Jones, D. L., Nanthakumar, K., Cox, B., Wehrens, X. H., Dorian, P., and Backx, P. H. (2015) Increased atrial arrhythmia susceptibility induced by intense endurance exercise in mice requires TNFα. *Nat. Commun.* **6,** 6018
8. Lugenbiel, P., Wenz, F., Govorov, K., Schweizer, P. A., Katus, H. A., and Thomas, D. (2015) Atrial fibrillation complicated by heart failure induces distinct remodeling of calcium cycling proteins. *PLoS ONE* **10,** e0116395
9. Richard, S., Leclercq, F., Lemaire, S., Piot, C., and Nargeot, J. (1998) Calcium currents in compensated hypertrophy and heart failure. *Cardiovasc. Res.* **37,** 300–311
10. Mukherjee, R., and Spinale, F. G. (1998) L-type calcium channel abundance and function with cardiac hypertrophy and failure: a review. *J. Mol. Cell. Cardiol.* **30,** 1899–1916
11. Splawski, I., Timothy, K. W., Sharpe, L. M., Decher, N., Kumar, P., Bloise, R., Napolitano, C., Schwartz, P. J., Joseph, R. M., Condouris, K., Tager-Flusberg, H., Priori, S. G., Sanguinetti, M. C., and Keating, M. T. (2004) Ca(V)1.2 calcium channel dysfunction causes a multisystem disorder including arrhythmia and autism. *Cell* **119,** 19–31
12. Splawski, I., Timothy, K. W., Decher, N., Kumar, P., Sachse, F. B., Beggs, A. H., Sanguinetti, M. C., and Keating, M. T. (2005) Severe arrhythmia disorder caused by cardiac L-type calcium channel mutations. *Proc. Natl. Acad. Sci. U.S.A.* **102,** 8089–8096
13. Napolitano, C., and Antzelevitch, C. (2011) Phenotypical manifestations of mutations in the genes encoding subunits of the cardiac voltage-dependent L-type calcium channel. *Circ. Res.* **108,** 607–618
14. Colecraft, H. M., Alseikhan, B., Takahashi, S. X., Chaudhuri, D., Mittman, S., Yegnasubramanian, V., Alvania, R. S., Johns, D. C., Marbán, E., and Yue, D. T. (2002) Novel functional properties of Ca^{2+} channel β subunits revealed by their expression in adult rat heart cells. *J. Physiol.* **541,** 435–452
15. Van Petegem, F., Duderstadt, K. E., Clark, K. A., Wang, M., and Minor, D. L., Jr. (2008) Alanine-scanning mutagenesis defines a conserved energetic hot spot in the Cavα1 AID-Cavβ interaction site that is critical for channel modulation. *Structure* **16,** 280–294
16. Catterall, W. A. (2000) Structure and regulation of voltage-gated Ca^{2+} channels. *Annu. Rev. Cell Dev. Biol.* **16,** 521–555
17. Peterson, B. Z., DeMaria, C. D., Adelman, J. P., and Yue, D. T. (1999) Calmodulin is the Ca^{2+} sensor for Ca^{2+}-dependent inactivation of L-type calcium channels. *Neuron* **22,** 549–558
18. Dolphin, A. C. (2009) Calcium channel diversity: multiple roles of calcium channel subunits. *Curr. Opin. Neurobiol.* **19,** 237–244
19. Gao, T., Puri, T. S., Gerhardstein, B. L., Chien, A. J., Green, R. D., and Hosey, M. M. (1997) Identification and subcellular localization of the subunits of L-type calcium channels and adenylyl cyclase in cardiac myocytes. *J. Biol. Chem.* **272,** 19401–19407
20. Wu, J., Yan, Z., Li, Z., Qian, X., Lu, S., Dong, M., Zhou, Q., and Yan, N. (2016) Structure of the voltage-gated calcium channel Cav1.1 at 3.6 A resolution. *Nature* **537,** 191–196
21. Bourdin, B., Marger, F., Wall-Lacelle, S., Schneider, T., Klein, H., Sauvé, R., and Parent, L. (2010) Molecular determinants of the Cavβ-induced plasma membrane targeting of the Cav1.2 channel. *J. Biol. Chem.* **285,** 22853–22863
22. Fuller-Bicer, G. A., Varadi, G., Koch, S. E., Ishii, M., Bodi, I., Kadeer, N., Muth, J. N., Mikala, G., Petrashevskaya, N. N., Jordan, M. A., Zhang, S. P., Qin, N., Flores, C. M., Isaacsohn, I., Varadi, M., *et al.* (2009) Targeted disruption of the voltage-dependent calcium channel $\alpha2/\delta1$ subunit. *Am. J. Physiol. Heart Circ. Physiol.* **297,** H117–H124
23. Singer, D., Biel, M., Lotan, I., Flockerzi, V., Hofmann, F., and Dascal, N. (1991) The roles of the subunits in the function of the calcium channel. *Science* **253,** 1553–1557
24. Parent, L., Schneider, T., Moore, C. P., and Talwar, D. (1997) Subunit regulation of the humain brain α_{1E} calcium channel. *J. Membr. Biol.* **160,** 127–140
25. Bourdin, B., Shakeri, B., Tétreault, M. P., Sauvé, R., Lesage, S., and Parent, L. (2015) Functional characterization of $Ca_V\alpha2\delta$ mutations associated with sudden cardiac death. *J. Biol. Chem.* **290,** 2854–2869
26. Yasuda, T., Chen, L., Barr, W., McRory, J. E., Lewis, R. J., Adams, D. J., and Zamponi, G. W. (2004) Auxiliary subunit regulation of high-voltage activated calcium channels expressed in mammalian cells. *Eur. J. Neurosci.* **20,** 1–13
27. Tétreault, M. P., Bourdin, B., Briot, J., Segura, E., Lesage, S., Fiset, C., and Parent, L. (2016) Identification of glycosylation sites essential for surface expression of the Cav$\alpha2\delta1$ subunit and modulation of the cardiac Cav1.2 channel activity. *J. Biol. Chem.* **291,** 4826–4843

28. Wu, J., Yan, Z., Li, Z., Yan, C., Lu, S., Dong, M., and Yan, N. (2015) Structure of the voltage-gated calcium channel Cav1.1 complex. *Science* **350,** aad2395
29. Van Petegem, F., Clark, K. A., Chatelain, F. C., and Minor, D. L., Jr. (2004) Structure of a complex between a voltage-gated calcium channel β-subunit and an α-subunit domain. *Nature* **429,** 671–675
30. Segura, E., Bourdin, B., Tétreault, M. P., Briot, J., Allen, B. G., Mayer, G., and Parent, L. (2017) Proteolytic cleavage of the hydrophobic domain in the $Ca_V\alpha2\delta1$ subunit improves assembly and activity of cardiac $Ca_V1.2$ channels. *J. Biol. Chem.* **292,** 11109–11124
31. Voigt, A., Freund, R., Heck, J., Missler, M., Obermair, G. J., Thomas, U., and Heine, M. (2016) Dynamic association of calcium channel subunits at the cellular membrane. *Neurophotonics* **3,** 041809
32. Bourdin, B., Segura, E., Tétreault, M.-P., Lesage, S., and Parent, L. (2016) Determination of the relative cell surface and total expression of recombinant ion channels using flow cytometry. *J. Vis. Exp.* **115,** e54732
33. Sekine-Aizawa, Y., and Huganir, R. L. (2004) Imaging of receptor trafficking by using α-bungarotoxin-binding-site-tagged receptors. *Proc. Natl. Acad. Sci. U.S.A.* **101,** 17114–17119
34. Paxman, J. J., and Heras, B. (2017) Bioinformatics tools and resources for analyzing protein structures. *Methods Mol. Biol.* **1549,** 209–220
35. Creighton, T. E. (1993) *Proteins, Structure and Molecular Properties*, p. 141, W. H. Freeman & Co., New York
36. Hille, B. (1992) *Ionic Channels of Excitable Membranes*, Sinauer Associates, Inc., Sunderland, MA
37. Dolphin, A. C. (2016) Voltage-gated calcium channels and their auxiliary subunits: physiology and pathophysiology and pharmacology. *J. Physiol* **594,** 5369–5390
38. Dolphin, A. C. (2013) The $\alpha2\delta$ subunits of voltage-gated calcium channels. *Biochim. Biophys. Acta* **1828,** 1541–1549
39. Altier, C., Garcia-Caballero, A., Simms, B., You, H., Chen, L., Walcher, J., Tedford, H. W., Hermosilla, T., and Zamponi, G. W. (2011) The Cavβ subunit prevents RFP2-mediated ubiquitination and proteasomal degradation of L-type channels. *Nat. Neurosci.* **14,** 173–180
40. Shistik, E., Ivanina, T., Puri, T., Hosey, M., and Dascal, N. (1995) Calcium current enhancement by $\alpha2/\delta$ and β subunits in *Xenopus* oocytes: contribution of changes in channel gating and $\alpha1$ protein level. *J. Physiol.* **489,** 55–62
41. Bangalore, R., Mehrke, G., Gingrich, K., Hofmann, F., and Kass, R. S. (1996) Influence of L-type Ca channel $\alpha2/\delta$ subunit on ionic and gating current in transiently transfected HEK 293 cells. *Am. J. Physiol.* **270,** H1521–H1528
42. Savalli, N., Pantazis, A., Sigg, D., Weiss, J. N., Neely, A., and Olcese, R. (2016) The $\alpha2\delta1$ subunit remodels $Ca_V1.2$ voltage sensors and allows Ca^{2+} influx at physiological membrane potentials. *J. Gen. Physiol.* **148,** 147–159
43. Wolf, M., Eberhart, A., Glossmann, H., Striessnig, J., and Grigorieff, N. (2003) Visualization of the domain structure of an L-type Ca channel using electron cryo-microscopy. *J. Mol. Biol.* **332,** 171–182
44. Walsh, C. P., Davies, A., Butcher, A. J., Dolphin, A. C., and Kitmitto, A. (2009) Three-dimensional structure of CaV3.1. *J. Biol. Chem.* **284,** 22310–22321
45. Pantazis, A., Savalli, N., Sigg, D., Neely, A., and Olcese, R. (2014) Functional heterogeneity of the four voltage sensors of a human L-type calcium channel. *Proc. Natl. Acad. Sci. U.S.A.* **111,** 18381–18386
46. Shakeri, B., Bourdin, B., Demers-Giroux, P. O., Sauvé, R., and Parent, L. (2012) A quartet of leucine residues in the guanylate kinase domain of Cavβ determines the plasma membrane density of the Cav2.3 channel. *J. Biol. Chem.* **287,** 32835–32847
47. Dey, S., Pal, A., Chakrabarti, P., and Janin, J. (2010) The subunit interfaces of weakly associated homodimeric proteins. *J. Mol. Biol.* **398,** 146–160
48. Gonzalez, C., Contreras, G. F., Peyser, A., Larsson, P., Neely, A., and Latorre, R. (2012) Voltage sensor of ion channels and enzymes. *Biophys. Rev.* **4,** 1–15
49. Tuluc, P., Yarov-Yarovoy, V., Benedetti, B., and Flucher, B. (2016) Molecular interactions in the voltage sensor controlling gating properties of CaV calcium channels. *Structure* **24,** 261–271
50. Cantí, C., Nieto-Rostro, M., Foucault, I., Heblich, F., Wratten, J., Richards, M. W., Hendrich, J., Douglas, L., Page, K. M., Davies, A., and Dolphin, A. C. (2005) The metal-ion-dependent adhesion site in the von Willebrand factor-A domain of $\alpha2\delta$ subunits is key to trafficking voltage-gated Ca^{2+} channels. *Proc. Natl. Acad. Sci. U.S.A.* **102,** 11230–11235
51. Williams, M. E., Feldman, D. H., McCue, A. F., Brenner, R., Velicelebi, G., Ellis, S. B., and Harpold, M. M. (1992) Structure and functional expression of α_1, α_2, and β subunits of a novel human neuronal calcium channel subtype. *Neuron* **8,** 71–84
52. Wall-Lacelle, S., Hossain, M. I., Sauvé, R., Blunck, R., and Parent, L. (2011) Double mutant cycle analysis identified a critical leucine residue in IIS4-S5 linker for the activation of the Cav2.3 calcium channel. *J. Biol. Chem.* **286,** 27197–27205
53. Webb, B., and Sali, A. (2014) Protein structure modeling with MODELLER. *Methods Mol. Biol.* **1137,** 1–15
54. Shen, M. Y., and Sali, A. (2006) Statistical potential for assessment and prediction of protein structures. *Protein Sci.* **15,** 2507–2524
55. Afonine, P. V., Grosse-Kunstleve, R. W., Echols, N., Headd, J. J., Moriarty, N. W., Mustyakimov, M., Terwilliger, T. C., Urzhumtsev, A., Zwart, P. H., and Adams, P. D. (2012) Towards automated crystallographic structure refinement with phenix.refine. *Acta Crystallogr. D Biol. Crystallogr.* **68,** 352–367
56. Briot, J., D'Avanzo, N., Sygusch, J., and Parent, L. (2016) Three-dimensional architecture of the L-type calcium channel: structural insights into the Cav$\alpha2\delta1$ auxiliary protein. *Biochem. Mol. Biol. J.* 2:3, 10.21767/2471–8084.100025
57. Lomize, M. A., Pogozheva, I. D., Joo, H., Mosberg, H. I., and Lomize, A. L. (2012) OPM database and PPM web server: resources for positioning of proteins in membranes. *Nucleic Acids Res.* **40,** D370–D376